Reply to Referee #1:

We would like to thank referee #1 for detailed comments that helped us to improve the manuscript. We have carefully considered each of the reviewer's comments in our revision. Our responses are provided below (the reviewer's comments are shown inline in italics).

Specific Comments: Line 42: CO has been used in transport studies in global models much farther back in time than indicated by the references used here. The Allen et al. (1996, JGR) should be included here.

Reply: Revised as suggested.

Section 2.2: The two models are driven by the same meteorology and have a number of similarities. The authors need to highlight the major differences between the two models, as this is sort of lost in the test. Perhaps highlight the model differences in a table. This is important because one of the major aspects of the paper is illustrating the difference in the CO results between models.

Reply: Thanks for this helpful comment. We have added one sub-section "2.2.3 Differences between GMI and GEOS-Chem" and one table (Table 1), together with Table 2 (original "Table 1") to highlight the major differences between the two models. The added section is as follows:

"To highlight the differences between the GMI and GEOS-Chem model run, we summarize their major differences in Table 1. In addition, we calculate the annual mean values and interannual standard deviations of CO budget (including biofuel and fossil fuel emissions, biomass burning emissions, tropospheric chemical production, tropospheric methane oxidation, loss with tropospheric OH, and net transport from troposphere to stratosphere) for GMI and GEOS-Chem during the period 2004–2012, and the results are provided in Table 2. In general, CO emissions from fuel combustion and biomass burning are mostly the same, but the chemical production and loss rates of CO in the troposphere are quite different between the two models. Specifically, GEOS-Chem is 40%, 16% and 15% higher than GMI in tropospheric chemical production Of CO, tropospheric CH4 oxidation and CO loss with tropospheric OH, respectively. For the net CO transport from troposphere to stratosphere, GEOS-Chem is ~9.5% larger than GMI."

Line 164: NCAR convection scheme. Is this correct? If so, what scheme is this? Is there a reference? Rain, cloud, land-water-ice all come from MERRA. They are not calculated in GMI as implied by this sentence.

Reply: We have revised this sentence to "Convective transport of trace gases is parameterized using a modified CONV_TRAN routine contained in the NCAR CCM3 physics package (Kiehl et al., 1998)."

Kiehl, J. T., Hack, J. J., Bonan, G. B., Boville, B. A., Williamson, D. L., and Rasch, P. J.: The National Center for Atmospheric Research Community Climate Model: CCM3, J. Clim., 11(6), 1131–1149, 1998.

Line 167: Need another sentence here: …. hindcast spinup period. Therefore, the GMI simulation used in this analysis is for 2004 through 2012.

Reply: Revised as suggested.

Lines 218-219: Is it the monthly means that are archived?

Reply: Yes, they are monthly mean data.

Line 241: The headings in Table 2 are incorrect. "Minimum" should be "Maximum" and vice versa. What is meant by "peak" here? Is it the maximum of the grid cell values of monthly means?

Reply: The "Minimum" and "Maximum" refer to the absolute percentage differences between models and MLS observations, we have exchanged them and renamed to "Minimum difference" and "Maximum difference". The "peak" is the maximum grid cell value of seasonal means, we have changed to "peaks of simulated CO concentrations" to avoid confusion.

Line 254: Need to point out that this maximum is not as broad as in the MLS data.

Reply: Revised as "However, this maximum in model simulations is not as broad as in the MLS observations. In addition, both models underestimate CO concentrations poleward of 50°."

Line 270: …local maxima and minima…

Reply: Revised as suggested.

Line 271: …underestimation of CO extremes from GMI….

Reply: Revised as suggested.

Line 294: The underestimate over and downwind of North America should also be mentioned.

Reply: Revised as: "This is mainly due to the underestimated CO over South Asia and East Asia, as well as East US and downwind region as shown in Figure 1."

Line 323: At 147 hPa (not shown)….

Reply: Revised as suggested.

Line 347: 20 hPa

Reply: Revised to "…the same altitude (~50 hPa or 20 km)".

Line 378: It is unclear as to whether the underestimates listed here are for a particular month or an average over the years.

Reply: It is for a month (averaged over 8 years). We have revised to "The largest underestimation for a month by GMI…" to avoid confusion.

Lines 392-393: The peak in both models is a month later than MLS in East Asia also.

Reply: We have revised as: "Over the other three regions, simulated seasonal variations are not consistent with MLS. For example, MLS shows CO peaks in July for East Asia and in August for South Asia (Figs. 12d and 12e), but the peaks in both models lag MLS by one month."

Line 404: Note that the seasonal cycle is not correct in North Africa and South Asia.

Reply: We added one sentence: "…but large discrepancies exist over northern Africa and South Asia (Figs. 13c and 13e)."

Line 419: "largest at 215 hPa" This is not true for four regions in DJF and MAM where the difference maximizes at 100 hPa.

Reply: Thanks for pointing out this. We have checked the differences and revised as: "In general, the differences between GMI and GEOS-Chem are largest at 215 hPa (up to 19%) during DJF, whereas the differences reach maximum at 100 hPa (up to 13%) during JJA."

Line 466: "....which is also captured in the GMI simulation, but not in the GEOS-Chem simulation."

Reply: Revised as suggested.

Lines 474-475: I would say it is more pronounced at 215 than at 147 hPa.

Reply: Revised as suggested.

Lines 514-516: Is there any explanation for this poor behavior by the models?

Reply: The inconsistency over East Asia and South Asia between models and MLS observation may result from several reasons, including low biases in direct surface emission, the fraction of CO emissions released above the boundary layer, biogenic NMVOC oxidation, horizontal advection of CO, and model parameterizations of convective transport.

Lines 534-537: I don't think this conclusion is mentioned anywhere else in the paper.

Reply: We have revised as: "The UTLS transport of CO from East Asia across the Pacific to North America in MAM and JJA is shown in the two models' simulation, but the CO concentrations are much lower than observed by MLS."

Lines 591-593: This conclusion supports the need to have a table that clearly shows the differences between the two models, especially with respect to these topics.

Reply: We agree to this comment and please see our reply to the 2nd comment above.

Line 627: V4 CO is slightly more realistic

Reply: Revised as suggested.

Table 2: There needs to be an overall heading over the nine columns to the right of the correlations. It should say "Model Biases (%)".

Reply: Revised as suggested.

Reply to Referee #2:

We would like to thank referee #2 for detailed comments that helped us to improve the manuscript. We have carefully considered each of the reviewer's comments in our revision. Our responses are provided below (the reviewer's comments are shown inline in italics).

Much of the paper (Sections 3 4) focuses on comparing different features in the observations to the two simulations. However, these comparisons are largely descriptive (and often qualitative). Section 5 begins to address the causes for the differences, but doesn't go very far (particularly in terms of inter-model differences). As the authors point out, the two models are very similar because they use the same meteorology and emissions. This means the places where they differ would present a very nice opportunity to understand which processes contribute to the differences, but there is very little discussion of this. For example, why is GEOS-Chem generally higher at 100 hPa but lower at 215 hPa? Is it differences in the convective transport parameterisations in the two models? Differences in chemical production or loss in the UT, or loss in the LS? What else could be driving these differences? This would also require a more thorough accounting of the similarities and differences between the models (e.g. how do chemical schemes differ? How similar are convective parameterisations? etc.) Without this level of analysis, it feels a little like an opportunity to deepen our understanding has been lost.

Reply: We agree that understanding the processes contributing to the differences between MLS observation and model simulations, as well as the inter-model differences is important, especially for improving model parameterization and simulations in the future. However, it is beyond the scope of this study which aims to evaluate the CO concentration and its distribution and variation in the UTLS simulated by two CTMs using the latest version (V4.2) of Aura MLS data. The factors accounting for model-observation and inter-model differences can be quite complicated, including biases in direct surface emission, the fraction of CO emissions released above the boundary layer, biogenic NMVOC oxidation, horizontal advection of CO, and model parameterizations of convective transport. We do plan to study such processes and factors in another work, but not in the current paper. In our original manuscript, Table 2 did provide some insights on the inter-model differences in terms of CO budget, such as chemical production and loss rates of CO in the troposphere, which help to explain some of the discrepancies between the two model simulations. In the revised manuscript, we have added one sub-section "2.2.3 Differences between GMI and GEOS-Chem" and one new table (Table 1), together with Table 2 (original "Table 1") to highlight the major differences between the two models. The added section is as follows:

"To highlight the differences between the GMI and GEOS-Chem model run, we summarize their major differences in Table 1. In addition, we calculate the annual mean values and interannual standard

deviations of CO budget (including biofuel and fossil fuel emissions, biomass burning emissions, tropospheric chemical production, tropospheric methane oxidation, loss with tropospheric OH, and net transport from troposphere to stratosphere) for GMI and GEOS-Chem during the period 2004–2012, and the results are provided in Table 2. In general, CO emissions from fuel combustion and biomass burning are mostly the same, but the chemical production and loss rates of CO in the troposphere are quite different between the two models. Specifically, GEOS-Chem is 40%, 16% and 15% higher than GMI in tropospheric chemical production Of CO, tropospheric CH4 oxidation and CO loss with tropospheric OH, respectively. For the net CO transport from troposphere to stratosphere, GEOS-Chem is ~9.5% larger than GMI."

On a related note, I find Sections 3-4 long and hard to parse. Some sub-sections would help, especially in Section 3. There are a lot of qualitative descriptions of features in the figures, paired with phrases like "[Feature X] in the GMI simulation is more consistent with MLS observations than in the GEOS-Chem simulation" – but these are hard to judge from the figures and often not backed up with quantitative information. In many cases, (e.g. Figs 1-3, possibly 4-11 as well) it would be easier to follow the text descriptions if the figures showed for the model differences plots (e.g., GMI – MLS and GEOS-Chem – MLS) rather than absolute concentration plots. The absolute plots could go into a supplement as the paper is already long and contains many figures. It would also be nice if some of the statements could be quantified using e.g. regional or temporal averages, or even mean difference statistics over all grid squares.

Reply: Thanks for these helpful comments. In the revised manuscript, we have made major changes which include:

1. We divided Section 3 into three sub-sections: "Seasonal Distributions of CO in the UTLS", "Monthly Variations of CO in the UTLS", and "CO 'Tape Recorder'". Section 4 is divided into two sub-sections: "Monthly Variations of CO in the UTLS" and "Vertical Profiles of CO in the UTLS".

2. We plotted figures of the differences between the two models' simulations and MLS observations. Since we want to highlight the spatial and temporal patterns of model simulated CO, we think it is better to put the difference figures in the supplement (Figures S1-S11 corresponding to Figures 1-11 in the original manuscript).

3. We have added more quantitative discussion about the comparison between model simulations and MLS observations following the reviewer's suggestion. More statistic values are computed, such as correlation coefficient, maximum, minimum and mean values.

My final major concern is that the paper doesn't reference much recent literature. Of the 11 referenced papers published since 2011, 7 were led by authors from this paper. There is significant newer literature surrounding, for example, injection of trace gases to the UTLS in the Asian monsoon (e.g., Park et al., 2009; Randel et al., 2010; Randel and Jensen 2013). There is also newer literature on CO distributions, including in the upper troposphere, than the 2006 Shindell work cited here (e.g., Naik et al., 2013; Fisher et al., 2015; Zeng et al., 2015).

Reply: Thanks for this comment. We have searched and added more recent literature (including these mentioned by the reviewer) and discussions about related references in our revised manuscript.

Minor Comments (by line)

163: "climatological" CH4 files – are these year-specific, and if not do is a trend imposed?

Reply: Sorry for confusion. We have revised this sentence to "Surface methane is read from monthly mean distributions interpolated from NOAA flask observations, and allowed to advect and react".

200-201: Are biogenic emission calculations the same between models? GMI section references Guenther; GEOS-Chem section refers to MEGAN. Theoretically these are the same but the implementation could vary. In general it would be really nice to see what exactly is same vs. different between the models (see above).

Reply: The biogenic emission is similar between GMI and GEOS-Chem. For the model differences, please refer to our reply above.

224-225: Are MLS averaging kernels and a priori profiles time-varying or constant?

Reply: MLS averaging kernels are constant, they were obtained from MLS website (http://mls.jpl.nasa.gov/data/ak/). MLS *a priori* profiles are time-varying. In MLS Version 4 data, all the standard product files now include the *a priori* information used in the retrieval (as an additional "swath").

243-244: How do you know trans-Pacific transport from East Asia is weaker in the models? If just judging from the figure, couldn't it just be that the East Asian CO is lower to begin with? Can this be quantified? (e.g. relative difference between East Asia East Pacific?)

Reply: We agree with the reviewer that the simulated CO concentration at the beginning of the transport is much lower than the observation. We checked and confirmed that the models did reproduce the transport. Thus, we have revised the text to: "The trans-Pacific transport of CO from East Asia in MAM and JJA to North America is shown in the model simulations, but the CO concentrations are ~30% lower than the observations."

323: What does "well captured" mean here? To me it looks like models are quite a lot lower (relative difference would help)

Reply: Over Indonesia during 2006-07 El Niño, model simulated CO maxima are similar to MLS observation (relative difference < 5%). We have revised the text to "The maxima (~160–170 ppbv) over Indonesia during 2006-07 El Niño are well captured by the models (difference between model and observation < 5%)."

391: "Remaining two" isn't quite right here as only 3 of 6 regions have been discussed so far in this paragraph (no mention of East Asia).

Reply: This issue is fixed in our revised manuscript.

421: Should "less than" be "greater than" here?

Reply: Yes and it is corrected in the revision.

453-454: Stating that the MLS IWC and modelled convective mass flux have "good linear correlation" is unsatisfying. Given how importance the simulation of convective transport is for this region of the troposphere, it would be really nice to show this comparison to the reader (perhaps in the supplement), or at least quantify it.

Reply: We have added a scatter plot (Fig. S12) in the supplement showing the linear correlation between MLS IWC and model convective mass flux. The correlation coefficients are also added in the revised manuscript to quantify the relationship.

Table 1: Does "tropospheric chemical production" really mean tropospheric chemical production from NMVOCs, or does this include the CH4 contribution? Please clarify.

Reply: Tropospheric chemical production includes both CH4 and NMVOC oxidation. To avoid confusion, we have restyled the original Table 1 as below:

Model		GMI	GEOS-Chem
Biofuel + Fossil Fuel		20.6 ±0.16	19.6 ±0.29
Biomass Burning		11.9 ±1.9	11.9 ±2.0
Tropospheric Chemical Production		42.3 ±0.92	59.1 ±0.77
	Source from Methane Oxidation	30.3 ±0.95	35.2 ±0.42

Loss with Tropospheric OH	77.7 ±2.1	89.1 ±2.4
Net Transport to Stratosphere	1.37 ±0.49	1.50 ±0.47

Figs 12-13: Since error bars are interannual standard deviations (not measurement errors) and simulations cover same period as observations, why not show these for the models as well?
Reply: The error bars are added for the two models in the revision.

Fig 14: For the analysis, it would be helpful to also show (or in a separate figure) the full vertical profiles from the surface. This would help determine whether the differences seen starting at 215 hPa are there because the two models start with different surface values, or because they are vertically transporting the CO to different altitudes (e.g. maybe there is more GEOS-Chem CO at 300 hPa), or something else.
Reply: We agree that it would be helpful to show the full vertical profiles for comparison between models and observation. However, MLS is only sensitive to CO at 215 hPa and above, the CO profile below (i.e., pressures greater than) 215 hPa is not reliable. The two models have different pressure levels, and the model simulated CO profiles are interpolated to the pressure levels of the MLS observation by using MLS CO averaging kernels and a priori profiles. Thus, such comparison may be done in future work using satellite retrieved or ground-based measurement of full vertical profile.

Evaluation of UTLS carbon monoxide simulations in GMI and GEOS-Chem chemical transport models using Aura MLS observations

Lei Huang[1], Jonathan H. Jiang[1], Lee T. Murray[2,3], Megan R. Damon[4], Hui Su[1], Nathaniel J. Livesey[1]

[1] {Jet Propulsion Laboratory, California Institute of Technology, Pasadena, CA}

[2] {NASA Goddard Institute for Space Studies, New York, NY}

[3] {Lamont-Doherty Earth Observatory, Columbia University, Palisades, NY}

[4] {NASA Goddard Space Flight Center, Greenbelt, MD}

Correspondence to: Lei Huang (Lei.Huang@jpl.nasa.gov)

Formatted: Font: 12 pt

Abstract

This study evaluates the distribution and variation of carbon monoxide (CO) in the upper troposphere and lower stratosphere (UTLS) during 2004–2012 as simulated by two chemical transport models, using the latest version of Aura Microwave Limb Sounder (MLS) observations. The simulated spatial distributions, temporal variations and vertical transport of CO in the UTLS region are compared with those observed by MLS. We also investigate the impact of surface emissions and deep convection on CO concentrations in the UTLS over different regions, using both model simulations and MLS observations. Global Modeling Initiative (GMI) and GEOS-Chem simulations of UTLS CO both show similar spatial distributions to observations. The global mean CO values simulated by both models agree with MLS observations at 215hPa and 147 hPa, but are significantly underestimated by more than 40% ~~(> 40%)~~ at 100 hPa. In addition, the models underestimate the peak CO values by up to 70% at 100 hPa, 60% at 147 hPa, and 40% at 215hPa, with GEOS-Chem generally simulating more CO at 100 hPa and less CO at 215hPa than GMI. The seasonal distributions of CO simulated by both models are in better agreement with MLS in the Southern Hemisphere (SH) than in the Northern Hemisphere (NH), with disagreements between model and observations over ~~some~~ enhanced CO regions such as southern Africa. The simulated vertical transport of CO shows better agreement with MLS in the tropics and the SH subtropics than the NH subtropics. We also examine regional variations in the relationships among surface CO emission, convection and UTLS CO concentrations. The two models exhibit emission-convection-CO relationships similar to those observed by MLS over the tropics and some regions with enhanced UTLS CO.

1 Introduction

Carbon monoxide (CO) plays ~~multiple~~ important roles in atmospheric chemistry and radiation balance. In particular, it serves as the primary sink of the hydroxyl radical (OH) (Logan et al., 1981) and is an important tropospheric ozone (O_3) precursor (Daniel and Solomon, 1998). CO in the troposphere is mostly emitted from the surface as a byproduct of incomplete combustion of carbon-based fuels, and it has primary sources from fossil fuel and biomass burning as well as secondary sources from oxidation of methane and other hydrocarbons (Jacob, 1999; Shindell et al., 2006). CO can be rapidly uplifted into mid- and upper troposphere by convection, where it can be transported around the globe (Jiang et al. 2007). With a typical lifetime of 1–2 months in the troposphere, CO has been often used as a tracer for studying the transport of polluted air masses that originate in regions of biomass burning or fossil fuel combustion (e.g., Allen et al., 1996; Edwards et al., 2006, Huang et al., 2012).

Previous studies using both satellite observations and model simulations have shown that CO has strong seasonal and interannual variations in the upper troposphere and lower stratosphere (UTLS) (e.g., Schoeberl et al., 2006; Liu et al., 2007; Liu et al., 2010, 2013; Huang et al., 2012, 2014). Temporal variations of CO in the UTLS are affected by many factors, including surface emission and convection, each havings different seasonal variations; as well as photochemistry and transport, which can affect CO concentrations either locally or across a long -distance. Schoeberl et al. (2006) studied vertical transport of CO across UTLS by analyzing the "tape recorder" - the vertical and temporal variations of CO observed by the Aura Microwave Limb Sounder (MLS) during August 2004 to December 2005. Their study indicates that ~~this~~ the CO "tape recorder" arises

from combined seasonal variations in both surface emissions and convective transport of CO into the upper troposphere (UT). These can be simulated by the Global Modeling Initiative (GMI) chemical transport model (CTM) forced by climatological emissions. Many other studies also have shown that convolved ~~seasonalit~~seasonality~~y~~ in surface emissions and deep convective activity jointly produce ~~combines to~~ enhanced CO fluxes from the surface to the UT resulting in seasonal peaks of CO (e.g., Liu et al., 2007; Liu et al., 2010; Huang et al., 2012). Strong interannual variation of CO in the UT has been found to be mainly associated with intense drought-induced fires in Indonesia and South America during El Niño periods (Liu et al., 2013; Livesey et al., 2013; Huang et al., 2014).

Although both surface emissions and convective transport could influence the seasonal peaks of CO in the UTLS, the relative importance of each factor varies between regions. Liu et al. (2007) suggested that high CO concentrations in the tropical UT during boreal Spring are mainly caused by a number of intense convective events over Africa and the Amazon that transport large amounts of fire-generated CO to the tropical tropopause layer. Ricaud et al. (2007) found that the peak in CO at the tropopause over Africa during boreal Spring largely results from convective and large-scale horizontal transport pathways, regardless of source region. Further study by Huang et al. (2012) confirmed that the locations and seasonality of the UT CO maxima in the tropics were strongly correlated with the frequency of local convection over South America and Central Africa during 2007. However, Schoeberl et al. (2006), using model simulations, argued that the UT CO maximum mainly results from strong biomass burning in Indo-C~~e~~hina. Gonzi and Palmer (2010) further found that the fractions of surface CO

emissions transported to the UT are lower over Africa and South America than over Indonesia during June to October 2006. Although the relationships among emissions, convection, dynamical transport and UTLS CO abundance have been investigated by some observational studies (e.g., Jiang et al., 2007; Huang et al., 2012; Livesey et al. 2013), it is still not clear whether models can reproduce these relationships.

The ability of global CTMs to capture the processes driving CO temporal and spatial variations needs to be evaluated with observations. However, most of the previous model evaluation studies have been limited to comparison with in-situ surface observations~~data~~ (e.g., Duncan et al., 2007), in-situ aircraft field campaigns with limited spatial and temporal coverage (e.g., Hudman et al., 2007; Fisher et al., 2015), and ground- or satellite-based remotely sensed total column or coarse resolution vertical profile data (e.g., Edwards et al., 2006; Gloudemans et al., 2006; De Laat et al., 2007; Naik et al., 2013; Zeng et al., 2015). There are also some model inversion studies on CO sources (e.g., Heald et al., 2004; Kopacz et al., 2009), including a few studies using vertical CO information from multiple satellite products (e.g., Kopacz et al., 2010). Shindell et al. (2006) evaluated seasonal and spatial distributions of surface CO in 26 global atmospheric chemistry models and found that these models generally underestimate extratropical CO concentration in the Northern Hemisphere, although they typically perform reasonably well elsewhere. Fisher et al. (2015) showed large variabilities in the ability of different models to reproduce the observed CO profiles, and more complex chemical mechanisms do not necessarily produce more accurate simulation of CO vertical gradients. Zeng et al. (2015) compared simulated CO to observations from ground-based total column measurements at selected Southern Hemisphere (SH) sites and

found that accurate representation of biogenic emissions is critical to reproducing observed SH background CO. Although total column comparisons provide an advantage over in-situ surface comparisons for model validation in the free troposphere, neither surface nor total column data were able to constrain the vertical structure of CO in the models. Since 2004, the MLS instrument aboard the Aura satellite has been providing ~~CO~~ vertical profile measurements of various trace gases (e.g., CO, H_2O, O_3) in the UTLS, which have been widely used for ~~CO~~ trace gas distribution and transport studies (e.g., Park et al., 2009; Liu at al., 2010, 2013; Randel et al., 2010; Huang et al, 2012, 2014; Randel and Jensen, 2013). For example, Park et al. (2009) studied the source and transport of CO in the Asian monsoon circulation by using chemistry transport model simulation and MLS observation. Randel et al. (2010) identified the transport of polluted air masses from the surface to the stratosphere during Asian monsoon season by using MLS observation of hydrogen cyanide (HCN). Liu et al. (2010) evaluated CO transport in the GEOS-Chem CTM driven by GEOS-4 and GEOS-5 assimilated meteorological fields and discussed the differences with MLS observations. Huang et al. (2012, 2014) developed a method to automate the identification of convective transport pathways of CO through a joint use of MLS and A-Train satellite measurements and applied this method to study factors affecting the seasonal and interannual variations of tropical UT CO.

This study aims to evaluate the CO concentration and its distribution and variation in the UTLS during 2004–2012 simulated by two state-of-the-~~science~~ art CTMs using the latest version (V4.2) of Aura MLS data. The two models we use are GMI and GEOS-Chem. We will investigate whether the models can reproduce the relationships

Formatted: Subscript

Formatted: Subscript

between surface CO emissions, convection and UTLS CO concentration seen in proxy and direct observations. Section 2 introduces the Aura MLS data and model simulations used. Section 3 compares model-simulated climatological seasonal distributions, monthly variations and tape recorder signal of CO in the UTLS with the MLS observations. Section 4 analyzes and discusses the discrepancies in CO in the UTLS over selected regions between the model simulations and MLS observations. Section 5 investigates the convolved impacts of CO emissions and convection on UTLS CO concentrations in both the satellite observation and model simulations. The main conclusions of this study are summarized and discussed in Section 6.

2 Data

2.1 Aura MLS Observations

The MLS instrument aboard the Aura satellite was launched on 15 July 2004. Aura has a sun-synchronous orbit at an altitude of 705 km, with equatorial crossing times at 1:45 a.m. and 1:45 p.m. local solar time and a 16-day repeat cycle. MLS makes measurements of atmospheric composition, temperature, humidity and cloud ice in the upper troposphere and stratosphere by measuring thermal microwave emissions from broad spectral bands with a limb-viewing geometry (Waters et al., 2006). An advantage of MLS is that its measurements can be obtained in the presence of ice clouds and aerosols that prevent measurements by shorter wavelength infrared, visible and ultraviolet techniques. MLS observes CO at 240 GHz, with a vertical resolution of ~5 km in the UTLS and horizontal resolutions of ~6 km and 500–600 km across- and along-track, respectively (Livesey et al., 2008). An earlier version of the MLS CO retrieval (V2.2) was biased high by a factor of two at 215 hPa, although the morphology was generally

148 realistic (Livesey et al., 2008). In a later version (V3.3), the high positive bias at 215 hPa
149 was removed, but the impact of deep clouds on CO obervations was considerably worse
150 (Livesey et al., 2011). The newest version (V4.2) of the MLS data (Livesey et al. 2015)
151 was released in July 2015, reduces the cloud impacts seen in V3.3 while avoiding the
152 biases associated with V2.2. Comparisons of UTLS CO between the new (V4.2) and
153 previous (V3.3) versions are discussed in Appendix A (Figs. A1 and A2). Only thick
154 clouds that are typically associated with deep-convective cores are observable by MLS
155 (Wu et al., 2008), thus MLS cloud ice water content (IWC) has been used as a proxy of
156 deep convection in previous studies (e.g., Jiang et al., 2011; Liu et al., 2013; Livesey et al.
157 2013). In this study, we use MLS V4.2 Level 2 CO and IWC data, screening the data
158 using recommended procedures (Livesey et al., 2015). The lowest usable retrieval level
159 for CO and IWC is 215 hPa, where the estimated single-measurement precisions are ~19
160 ppbv for CO and ~1.2 mg m^{-3} for IWC. The systematic uncertainty for CO at 215 hPa is
161 ±30 ppbv and ±30%, and generally ±30% at other UTLS pressure levels (Livesey et al.,
162 2015).

163 ## 2.2 GMI and GEOS-Chem Model Simulations

164 **2.2.1 GMI Model**

165 The GMI is a global 3-D CTM that includes full chemistry for both the troposphere
166 and stratosphere. The GMI model is an assessment tool as part of the NASA Modeling,
167 Analysis, and Prediction (MAP) program. It is capable of multiyear simulations for
168 assessments of anthropogenic impacts on atmospheric composition and the role of
169 long-range transport of pollution (Rotman et al., 2001). The GMI model includes a
170 combined stratosphere-troposphere chemical mechanism with 124 species, 320 chemical

reactions, and 81 photolytic reactions. The chemical mechanism in the troposphere includes a detailed description of tropospheric ozone, NO_x, and hydrocarbon photochemistry (Bey et al., 2001a). Photolysis rates in the troposphere and stratosphere are calculated by using the Fast-JX radiative transfer algorithm (Wild et al., 2000; Bian and Prather, 2002), which is an efficient algorithm for calculating photolysis rates in the presence of clouds and aerosols. Radiative and heterogeneous effects of aerosols on photochemistry are included in this model. Biogenic emissions of isoprene and monoterpenes are calculated online (Guenther et al., 2006). Surface methane is read from climatological monthly files, and allowed to advect and react. Convective transport of trace gases is parameterized using a modified CONV_TRAN routine contained in the NCAR CCM3 physics package (Kiehl et al., 1998)~~the NCAR convection scheme (rain, cloud, and land water ice are calculated online)~~.

The time period of the GMI hindcast simulation is 1990–2012, with 1990–1994 considered as the hindcast spinup period. Therefore, the GMI simulation used in this analysis is for 2004 through 2012. The meteorological fields are from the Global Modeling and Assimilation Office (GMAO) Modern-Era Retrospective Analysis for Research and Applications (MERRA) reanalysis (Rienecker et al., 2011). The MERRA data have 72 vertical levels with a top at 0.01 hPa, and the horizontal resolution is $1/2^\circ$ latitude $\times$ $2/3^\circ$ longitude, which has been degraded to 2° latitude $\times$ 2.5° longitude for input to the CTM. The biomass burning (BB) emissions used in the simulation are from the Global Fire Emission Database version 3 (GFED3) (van der Werf et al., 2010). The fossil fuel (FF) emissions are based on the Emission Database for Global Atmospheric Research (EDGAR) v3.2 inventory for 2000, overwritten with regional inventories over

194 specific regions (Zhang et al. (2009) inventory for 2006 over Asia, EPA NEI 2005 over
195 USA, EMEP over Europe, BRAVO over Mexico, CAC over Canada). The year-to-year
196 variability in the FF emissions is calculated wherever the inventories have year-specific
197 information. Otherwise, scaling factors from GEOS-Chem model (van Donkelaar et al.,
198 2008) are used to make the FF emissions year-specific. However, at the time when the
199 GMI emissions were generated, the GEOS-Chem scaling factors ended in 2006, so for
200 2007–2012, the USA emissions were scaled based on EPA emission totals for each year
201 and the European emissions were scaled on a country-wide basis using national emissions
202 from EMEP, and the Asian emissions were scaled using the REAS inventory projections.
203 Biofuel emissions are from Yevich and Logan (2003) and EPA emission inventory.

204 **2.2.2 GEOS-Chem Model**

205 GEOS-Chem is a global 3-D CTM developed by the atmospheric chemistry group at
206 Harvard University and has been widely used around the world. It is driven by
207 assimilated meteorological observations from the NASA GMAO Goddard Earth
208 Observing System (GEOS) (Bey et al., 2001b). GEOS-Chem includes a fully-coupled
209 treatment of tropospheric O_3-NO_x-VOC chemistry and various types of aerosols (e.g.,
210 Park et al., 2003; Alexander et al., 2005), along with 155 species, 292 chemical reactions,
211 and 64 photolytic reactions. Chemistry is fully resolved in the troposphere, with a
212 linearized scheme applied in the stratosphere (Murray et al., 2013). Emissions in
213 GEOS-Chem are from the same several basic inventories as used by GMI, with annual
214 scaling factors applied to account for trends. As for GMI, the Fast-JX radiative transfer
215 algorithm is used in GEOS-Chem. Anthropogenic non-methane volatile organic
216 compounds (NMVOCs) are emitted from the REanalysis of the TROpospheric chemical

composition (RETRO) inventory (Schultz et al., 2007), except for propane and ethane, which follow Xiao et al. (2008). Biogenic NMVOC emissions follow the Model of Emissions and GAses from Nature (MEGAN), which vary monthly with observations of leaf area indices from satellite and hourly with temperature, radiation, and precipitation (Barkley et al., 2011). Surface methane is read from monthly mean distributions interpolated from NOAA flask observations, and allowed to advect and react~~Surface methane concentrations are fixed each month to maps interpolated from NOAA flask data, and allowed to advect and subsequently react~~. Convective transport in GEOS-Chem is computed from the convective mass fluxes in the meteorological archive, as described by Wu et al. (2007). In this study, we use the simulations of GEOS-Chem version 9-02 (www.geos-chem.org) driven by MERRA reanalysis, the same meteorological fields as the GMI simulations. Vertical resolution is degraded from that of the MERRA inputs above 78.5 hPa but maintained at the MERRA resolution below, resulting in 47 total layers. The simulation period is 2003–2012, with January 2003 to April 2004 discarded as initialization. The model output data have a horizontal resolution of 2 ° latitude × 2.5 ° longitude, and 47 vertical layers between the surface and 0.01 hPa.

2.2.3 Differences between GMI and GEOS-Chem

To highlight the differences between the GMI and GEOS-Chem model run, we summarize their major differences in Table 1. In addition, we calculate the~~The 2004–2012~~ annual mean values and interannual standard deviations of CO budget (including biofuel and fossil fuel emissions, biomass burning emissions, tropospheric chemical production, tropospheric methane oxidation, loss with tropospheric OH, and net transport from troposphere to stratosphere) for GMI and GEOS-Chem during the period 2004–

2012, and the results are provided in Table ~~1~~2. In general, CO emissions from fuel combustion and biomass burning are mostly the same, but the chemical production and loss rates of CO in the troposphere are quite different between the two models. Specifically, GEOS-Chem is 40%, 16% and 15% higher than GMI in tropospheric chemical production Of CO, tropospheric CH4 oxidation and CO loss with tropospheric OH, respectively. For the net CO transport from troposphere to stratosphere, GEOS-Chem is ~9.5% larger than GMI.

2.2.~~4~~3 Model/MLS Comparison Approach

~~The 2004–2012 annual mean values and interannual standard deviation of CO budget for GMI and GEOS-Chem are provided in Table 1. In general, CO emissions from fuel and biomass burning are mostly the same, but the chemical production and loss rates of CO in the troposphere are quite different between the two models.~~ Both the GMI and GEOS-Chem simulations were archived at monthly temporal resolution, with the same horizontal resolution. GEOS-Chem provides model output on model levels whose pressure varies in time, whereas GMI provides output at fixed pressure levels. To compare the simulated and observed CO profiles, we first aggregate the daily Aura MLS along-track CO profiles into 2 ° latitude × 2.5 ° longitude grid boxes, and calculate monthly averages of CO in each grid box. We then apply the MLS V4.20 CO averaging kernels and a priori profiles to each model's simulated CO profiles to take into consideration the vertical sensitivity of the MLS retrieval for a most consistent comparison (Livesey et al., 2015). In this process, the modelled CO profiles are interpolated to the 37 pressure levels of the MLS retrieval.

3 Global Comparison between Models and Observation

~~3~~ 3.1 Seasonal Distributions of CO in the UTLS

Formatted: No bullets or numbering

Formatted: Font: 14 pt

The climatological seasonal distributions of CO at 215 hPa as observed by MLS and simulated by GMI and GEOS-Chem are shown in Figure 1 (the differences between model simulations and MLS observation are shown in Fig. S1). The seasonal average is calculated as the 8-year average from December 2004 to November 2012. In general, the locations of high CO are well simulated in GMI and GEOS-Chem versus the MLS observations, except over Africa. MLS indicates that local maxima occur over central Africa during DJF and southern Africa during SON (Huang et al., 2012), but the simulated maxima were over West Africa during both of these two seasons. The simulated CO values by both models are smaller than MLS observations, with an underestimation of generally less than 20% for the global mean (80°S–80°N) CO concentration (Table ~~2a~~3a). The largest underestimation occurs in MAM and JJA for both models, with GMI (GEOS-Chem) showing 20% (22.1%) and 20.2% (19.5%) less mean CO in MAM and JJA than MLS observations, respectively. Furthermore, peaks of simulated CO concentrations are smaller than MLS observations by up to ~40% for all seasons. The trans-Pacific transport of CO from East Asia in MAM and JJA to North America is ~~much weaker~~shown in the model simulations, but the CO concentrations are ~30% lower than ~~than shown in~~ the observations. Continental outflow of CO in the UT from the eastern US and West Africa to the Atlantic Ocean during JJA is also poorly simulated by both models. The simulated CO distribution of GMI is quite similar to that of GEOS-Chem (the correlation coefficient between the two maps for each season is greater than 0.98), with the difference of mean CO less than 7% (Table ~~2a~~3a). The mean and peak values of simulated CO in GEOS-Chem are generally less than those from GMI

at this level, especially over South America and Africa during DJF and SON (CO peak in GEOS-Chem is ~20% less than that in GMI).

At 147 hPa, high CO concentrations are mainly found in the tropical and sub-tropical latitudes, especially over South America and Africa (Figs. 2 and S2). During boreal Summer, there is a broad maximum over South Asia driven by convection associated with the Asian Summer monsoon (Fu et al., 2006; Park et al. 2009; Randel et al., 2010). However, this maximum in model simulations is not as broad as in the MLS observations. ~~Compared with MLS observations~~In addition, both models underestimate CO concentrations poleward of 50°. The underestimation is generally less than 32% for the global mean CO concentration (Table ~~2b~~3b), with the largest underestimation occurring in MAM for both models (32.4% for GMI, 31.5% for GEOS-Chem). In addition, seasonal CO maxima are also underestimated by about 30–40% in the tropics. The difference in mean CO concentration between the two model simulations is generally less than 5%, with GEOS-Chem slightly larger than GMI during all seasons except DJF (Table ~~2b~~3b). Maxima over South America and West Africa during SON and DJF are greater in magnitude (~15%) in GMI than in GEOS-Chem, but the latter shows a greater maximum (~9%) over South Asia during JJA than the former. The largest model-observation discrepancies occur at 100 hPa as shown in Figure 3 (and Fig. S3). Both models significantly underestimate the observed CO concentrations (note the different color scales in Fig. 3) compared to MLS. The underestimation is larger than 40% for the global mean CO concentration (Table ~~2c~~3c), with the largest underestimation occurring in MAM for both models (47.8% for GMI, 44.8% for GEOS-Chem). Although the simulations generally capture the local maxima and minima in each season, the

magnitudes are significantly smaller than the observation. The underestimation of CO extremes from GMI ranges from ~22% to ~70% compared with MLS CO, while the underestimation from GEOS-Chem ranges ~18–68%. Both model simulations show similar CO distributions to each other, but the CO maxima in GMI are generally smaller than those in GEOS-Chem, with a maximum difference of ~8.7% during JJA for the global mean CO (Table ~~2c~~3c).

The vertical distribution of zonal mean CO and its seasonal variations are shown in Figure 4 (and Fig. S4). In general, MLS CO shows a pipe-like maximum in the tropics from 200 hPa to 100 hPa, with a stronger vertical gradient above 100 hPa than below. However, the simulations have more diffuse horizontal gradients in the UT and the vertical gradient of CO is stronger below 100 hPa and weaker above 100 hPa than MLS. This may suggest that upward transport of CO is underestimated in the models. The average model bias (model CO minus MLS CO and then divided by MLS CO, same hereinafter) is -24 ~ -27% for GMI and -23 ~ -24% for GEOS-Chem throughout the year. The maximum model bias is -64% for GMI and -63% for GEOS-Chem. Although the models successfully reproduce a seasonal shift of local UT maxima from the tropics to the northern subtropics from DJF to JJA, they fail to simulate the higher maxima in the southern subtropics during SON. This is mainly due to the underestimation of CO concentration in the UT over southern Africa and South America (Figs. 1 and 2). The two models' simulations are quite similar (correlation coefficient > 0.996), except some differences in magnitude below (i.e., at pressures ~~larger~~ greater than) 150 hPa during SON and DJF as previously shown in the CO distribution map (Fig. 1).

3.2 Monthly Variations of CO in the UTLS

Formatted: Title, Left, Indent: First line: 0 ch, Space Before: 3 pt

Formatted: Font: 14 pt

The temporal variability of the zonal mean monthly CO from 30°S to 30°N at 215 hPa for more than 8 years (August 2004 – December 2012) is shown in Figure 5 (and Fig. S5). The high CO concentrations observed in the northern tropics and subtropics are underestimated in the models, especially from April to July when both models underestimate by as much as 33%, which is significant compared to the MLS measurement uncertainty. This is mainly due to the underestimated CO over South Asia and East Asia, as well as East US and downwind region as shown in Figure 1. As a consequence, the seasonal cycle of CO over this latitudinal band is not well simulated. The temporal variation of CO in the southern subtropics is well captured by GMI (r=0.83, n=15 latitudes × 101 months) and GEOS-Chem (r=0.80), except the magnitude is a little smaller than observation (difference < 10%). High CO values simulated by GMI during ENSO periods are comparable with MLS CO (difference is 2% - 11%), which is mainly related to stronger CO emissions generated by drought-induced fires in Indonesia or South America compared to normal years (Liu et al., 2013; Livesey et al., 2013; Huang et al., 2014). The maximum model bias at this level is -34% for GMI and -33% for GEOS-Chem, while the mean model bias is -9% (GMI) and -14% (GEOS-Chem). GMI shows higher CO values in the tropics during DJF and SON than GEOS-Chem (difference is still within 10%), especially in some El Niño-Southern Oscillation (ENSO) years –such as 2004-05, 2006-07 and 2010-11. The comparisons of zonal mean CO between MLS and models at 147 hPa are similar to 215 hPa (figure not shown). At 100 hPa (Figs. 6 and S6), the most distinctive feature is the semi-annual peaks with similar magnitudes in boreal Spring and Fall as shown in MLS data. This semi-annual variation of CO in the UT is mainly due to the temporal overlapping of surface biomass burning

from different continents and the inter-hemispheric shifts of deep convection (Duncan et al., 2007; Liu et al., 2013). The two models significantly underestimate CO at this level, and the peak during MAM is much weaker than the other peak during SON. The model bias ranges -54% ~ -22% for GMI and -48% ~ -13% for GEOS-Chem. The semi-annual CO peaks during boreal Spring and Fall in GEOS-Chem are slightly (~5%) larger than those in GMI.

Figure 7 shows the temporal evolution of monthly meridional mean tropical (15°S–15°N) CO at 215 hPa (also see Fig. S7). In general, GMI shows better agreement with MLS observation than GEOS-Chem with respect to the locations and magnitudes of the high CO concentration, since the magnitudes of CO peaks are 14% weaker in GEOS-Chem than in GMI. The correlation coefficients between observation and simulations are 0.78 and 0.81 for GMI and GEOS-Chem, respectively (n=144 longitudes × 101 months). The seasonal peaks over South America, Africa and Indonesia are well represented in the model simulations, but their magnitudes are smaller than those observed, especially over Africa and Indonesia (maximum bias is -42% for GMI and -51% for GEOS-Chem). The maxima (~160–170 ppbv) over Indonesia during 2006-07 El Niño ~~and over South America during 2010-11 La Niña~~ are well captured by the models (difference between model and observation < 5%). At 147 hPa (figure not shown), the interannual variation of meridional mean CO is similar to that at 215 hPa, except that the seasonal high CO encompasses a larger zonal area. At 100 hPa, the consistency between the models and MLS is substantially worse, as indicated by the significant underestimation (> 50%) of CO peaks and the locations of seasonal CO maxima (Figs. 8 and S8). For example, MLS shows a local CO maximum (~90 ppbv) over Africa during

November-December 2007 that the simulations do not capture. Furthermore, MLS detects clear semi-annual CO peaks over Africa, but the models only show one annual peak. The correlation coefficients between observation and simulations are also reduced to 0.74. Overall, the average magnitude of CO in GEOS-Chem is ~5% larger than that in GMI at this level.

3.3 CO "Tape Recorder"

Air masses can enter the stratosphere in the tropics, driven by adiabatic upwelling of the Brewer-Dobson circulation (Brewer, 1949). During this slow upward transport, seasonal and interannual variations in the mixing ratios of some trace gases are preserved, as first observed in water vapor by Mote et al. (1995). This phenomenon is termed the "tape recorder". Schoeberl et al. (2006) identified the CO tape recorder for the first time using MLS observations from August 2004 to December 2005. In this study, we evaluate the model-simulated CO tape recorder by taking advantage of the multi-year MLS data now available. Figure 9 shows the CO tape recorder over the tropics (as a zonal mean between 15 °S and 15 °N). An 8-year mean (2005–2012) was subtracted from the monthly mean time series at each level for MLS data and the two models' simulations. The differences of CO tape recorder between MLS observation and model simulations are shown in Figure S9. In general, the observed and simulated CO tape recorders show good agreement (r=0.76 for GMI, r=0.81 for GEOS-Chem, n=11 levels × 101 months). The observations and simulations show a semi-annual cycle around 200 hPa and a strong annual cycle above 80 hPa. In the lower stratosphere, both models show that the tape recorder signal fades out at approximately the same altitude (~50 hPa or 20 km) and the phase lines are quite similar to MLS observations. In the upper troposphere, the two

Formatted: Title, Left, Indent: First line: 0 ch, Space Before: 3 pt

Formatted: Font: 14 pt

models simulate the interannual variation of CO during the Northern and Southern Hemisphere fire seasons, which suggests that the surface CO emissions account for most of the CO variation near the tropopause. The phase shift and CO anomaly magnitude in GMI simulation are more consistent with MLS observation than those in GEOS-Chem simulation. For example, the average difference of positive CO anomaly between GMI and MLS is 15%, while that for GEOS-Chem is 32%. The models show that the location of the "tape head" is near 200 hPa, which is in rough agreement with MLS. In addition, the strong positive CO anomalies during three ENSO years (2004-05, 2006-07 and 2010-11) are captured by both observation and models.

The CO tape recorder signal over northern subtropics (10–30 °N) is shown in Figure 10 (also see Fig. S10). In general, model simulated tape recorders are not consistent with observation, as shown by a 2-3 month time lag between the same phases of CO peak anomaly. This inconsistency may be caused by the underestimation of vertical transport in the models (Schoeberl et al., 2006; Liu et al., 2010). Over this region, the ENSO signal is not as strong in the MLS observations as that over the tropics, yet the two models still show high positive CO anomalies during several ENSO periods. For the southern subtropics (10–30 °S), MLS and models have much better agreement (Figs. 11 and S11). The seasonal peaks and phase shift of CO anomalies are well collocated between observation and simulations. GMI simulation is much closer to MLS observation than GEOS-Chem in magnitude. For example, the difference of positive CO anomaly between GMI and MLS is within 31%, while that for GEOS-Chem is within 48%. However, the magnitude of positive anomaly in GMI simulation is still smaller than MLS observation

(except the 2006-07 El Niño year), which is mainly due to the underestimation of surface CO emission over South America and southern Africa (Liu et al., 2010, 2013).

4 Regional Comparison between Models and Observation

To further evaluate CO differences between observation and model simulations, we examine six regions of high CO: South America (0–30 °S, 40–80 °W), Southern Africa (0–30 °S, 10–40 °E), Northern Africa (0–30 °N, 15 °W–40 °E), East Asia (20–45 °N, 105–145 °E), South Asia (10–30 °N,70–105 °E), and Indonesia (10 °S–10 °N, 100–150 °E).

4.1 Monthly Variations of CO in the UTLS

Formatted: Title, Left, Indent: First line: 0", Space Before: 3 pt

Formatted: Font: 14 pt

Figure 12 shows the climatological monthly mean of CO at 215 hPa from MLS and the models over these regions. Both models underestimate the CO seen by the observations throughout the year over three regions (southern Africa, East Asia, and Indonesia). The largest underestimation for a month by GMI (GEOS-Chem) is 19% (33%) over South America, 30% (36%) over southern Africa, 22% (23%) over northern Africa, 37% (35%) over East Asia, 31% (29%) over South Asia, and 22% (22%) over Indonesia. The seasonal cycle of CO is similar between MLS and the models over South America (r=0.81 for both models), southern Africa (r=0.74 for GMI, r=0.75 for GEOS-Chem), ~~East Asia (r=0.76 for GMI, r=0.84 for GEOS-Chem)~~ and Indonesia (r=0.92 for GMI, r=0.95 for GEOS-Chem) (Figs. 12a, 12b, ~~12d~~ and 12f), although the magnitudes are underestimated. Over these first two regions, MLS shows maxima in October; both models greatly underestimate the peak value and fail to simulate the observed decreasing trend from October to January. Over Indonesia, there is an average underestimation of ~15% throughout the year. The underestimation of CO peaks over these regions may be due to low biases in direct surface emission, the fraction of fire emissions released above

the boundary layer, biogenic NMVOC oxidation, and/or upward convective transport. Over the ~~remaining~~ other ~~two~~ three regions~~, northern Africa and South Asia~~, simulated seasonal variations are not consistent with MLS. For example, MLS shows CO peaks in July for East Asia and in August for South Asia ~~–~~(Figs. 12~~d~~e and 12e), but the peaks in both models lag MLS by one month. This is probably due to insufficient representation of vertical transport in the CTMs or underlying meteorological reanalysis. CO mixing ratios simulated by GMI are generally larger than by GEOS-Chem, with differences typically less than 10%. However, the model differences are larger from October to February over South America and Africa, with a maximum of ~20% (Figs. 12a-c).

At 147 hPa, the differences in CO are similar to those at 215 hPa (figure not shown). Compared with MLS, the largest underestimation by GMI (GEOS-Chem) is 26% (32%) over South America, 35% (35%) over southern Africa, 28% (27%) over northern Africa, 33% (32%) over East Asia, 28% (25%) over South Asia, and 19% (18%) over Indonesia. The differences in CO at 100 hPa between MLS and the models are shown in Figure 13. The seasonal cycles are similar between MLS and models over South America, southern Africa and Indonesia (Figs. 13a, 13b and 13f), but large discrepancies exist over northern Africa and South Asia (Figs. 13c and 13e). The underestimation by the models reaches maximum at this level. For example, the largest underestimation by GMI is 46% over South America, 46% over southern Africa, 41% over northern Africa, 46% over East Asia, 42% over South Asia, and 36% over Indonesia, compared with MLS. In general, the temporal variations of GMI and GEOS-Chem are similar, but GMI is smaller than GEOS-Chem over all regions, especially from May to October.

4.2 Vertical Profiles of CO in the UTLS

Formatted: Title, Left, Indent: First line: 0", Space Before: 3 pt

Formatted: Font: 14 pt

To evaluate the vertical distribution of CO in the UTLS, we present 8-year seasonal mean CO profiles for each region (Fig. 14). Both models underestimate CO at all levels observed by MLS below (i.e., with pressures greater than) 50 hPa. The magnitude of underestimation depends on region, altitude and season. For instance, the difference between MLS and GMI CO during JJA increases monotonically from 215 hPa to 100 hPa over South America, whereas it first decreases (215 – 147 hPa) and then increases (147 – 100 hPa) over East Asia. This is also shown in earlier figures for the climatological monthly mean of CO in the UTLS (Figs. 12 and 13). In general, the differences between GMI and GEOS-Chem are largest at 215 hPa (up to ~~–~~198%) ~~and decrease with increasing altitude~~during DJF, whereas the differences reach maximum at 100 hPa (up to 13%) during JJA. GMI mixing ratios are greater than GEOS-Chem at altitudes below (i.e., pressures ~~less~~ greater than) 147 hPa over South America, Africa and Indonesia. However, it becomes slightly less than GEOS-Chem for heights above (i.e., pressures smaller than) 100 hPa. That the profile shapes are different, despite identical underlying meteorology, suggests that the way in which each CTM parameterizes its convective transport (including detrainment and entrainment) is affecting the resulting vertical distribution.

5 Relation between Emission, Convection and UTLS CO

In the sections above, we have evaluated the spatial distributions and temporal variations of CO in the UTLS simulated by the two models, on both the global and regional scale. Previous studies have shown that CO in the upper troposphere can be affected by both surface emission and convection (e.g., Schoeberl et al., 2006; Liu et al., 2007; Liu et al., 2010; Huang et al., 2012), thus it is important to evaluate the abilities of models to simulate the relationships between surface emission, convection, and CO in the

UTLS. In this way, we can better understand the differences between observation and simulation of CO in the UTLS.

The climatological monthly mean of surface CO emission from GMI (very similar to GEOS-Chem), IWC and CO at three pressure levels from MLS are shown in Figure 15. Each variable is normalized for comparison. MLS IWC is used here as a proxy of convective intensity ("CONV" in Fig. 15). In general, seasonality in CO at 147 hPa is similar to that at 215 hPa, but different from that at 100 hPa. The relationships between UTLS CO and emission and convection vary with regions. For example, over South America and southern Africa, the annual CO peak lags the emission peak by 1–2 months at 215 and 147 hPa. Over East and South Asia, the annual CO cycle closely follows the variation of convection at the two lower levels. Over northern Africa and Indonesia, it seems that both emission and convection are important in determining CO in the UTLS.

Due to the complexity of the emission-convection-CO relationship, we apply a bi-variate composite analysis (Jiang et al., 2007), and the results are shown in Figures 16 and 17 for CO at 215 hPa over the tropics (30°S–30°N) and different regions, respectively. The monthly mean CO mixing ratios at 215 hPa in each grid box from MLS observation and model simulations are binned according to the total (anthropogenic and biomass burning) surface CO emissions (x-axis) and the convective (CONV) index (y-axis). The CONV index is calculated as the IWC (from MLS observation) or convective mass flux (from two models' simulations) value in each grid box divided by the regional mean value at the same level. We have compared MLS IWC with convective mass flux from the models and found that they have good linear correlation (correlation coefficients > 0.7, as shown in Fig. S12). The surface CO emission data used for GMI

simulation are reused for the MLS bi-variate composite analysis. The color contour indicates the unity-based normalized CO value (i.e., 0 is the minimum and 1 is the maximum) at each pressure level.

Over the tropics (Fig. 16), MLS shows that CO concentration at 215 hPa is high when convection is strong. With the presence of deep convection (CONV > 1), CO generally increases with increasing surface emission. When convection is relatively weak (CONV < 0.1), CO is generally low and bears little connection with surface emission. CO concentration reaches maximum when both convection and emission are strong. When emission is very weak, the variation of CO may result from long-range transport preceding convective lofting (Huang et al., 2012). For example, MLS shows a high CO center when emission is relatively weak (between 0.02–0.1 g/m^2/month) and convection is strong (CONV > 2), which is also captured in the GMI simulation, but not in the GEOS-Chem simulation. In general, both GMI and GEOS-Chem simulations show similar emission-convection-CO relationships compared with MLS observation, except the slope of CO contours has some differences. For instance, GMI seems to overestimate CO when convection is moderate (0.05 < CONV < 1) or emission is strong (> 1 g/m^2/month), while GEOS-Chem underestimates CO when convection is strong (CONV > 1) with weak emission (< 0.1 g/m^2/month). At 147 hPa, the emission-convection-CO relationships are similar to those shown at 215 hPa. For MLS observations, CO increases with emission when convection is moderate or strong (CONV > 0.1), but the high CO ~~shown at 215 hPa~~ when emission is weak with strong convection is ~~less~~ more pronounced at 215 hPa than ~~this level~~147 hPa. The emission-convection-CO relationships simulated by GMI and GEOS-Chem also show similarity to MLS observation at 147 hPa, despite

some differences in the slope of CO contours. At 100 hPa, the emission-convection-CO relationships simulated by the two models are quite different from MLS observation (figure not shown), probably due to the significantly underestimated convection and CO in the models at this level, thus we do not discuss them in detail here. For the regional discussion below, we will also only focus on 215 hPa and 147 hPa.

Over the six different regions (Fig. 17), MLS shows that CO concentrations at 215 hPa are generally high when emission and convection are strong. However, there are also distinct regional differences. Over South America, CO does not change much when convection is relatively weak (CONV < 1), even though strong emission is present. CO increases rapidly when emission is large (> 1 g/m^2/month) with strong convection. This suggests that local convection plays an important role in determining CO mixing ratio in the UT over this region, which has been demonstrated by previous studies (e.g., Huang et al., 2012). Over southern and northern Africa, two high CO centers occur when convection is strong (CONV > 1), one is located in a weak emission regime (0.02–0.1 g/m^2/month), and the other is accompanied by strong emission (> 0.5 g/m^2/month). This is similar to the two CO centers at 215 hPa over the tropics (Fig. 16). It is noteworthy that there is a large CO difference between cases where emissions are 0.1 g/m^2/month and those with 0.5 g/m^2/month emissions over northern Africa, with the latter cases exhibiting larger CO. Over East and South Asia, CO concentration is high in all cases where deep convection is present (CONV > 1). Even when emission is weak (< 0.1 g/m^2/month), CO mixing ratio can still be high with strong convection, which suggests that CO transport by convection and advection may be important over this region. During the Asian Summer monsoon season, CO emitted from northeast India and southwest China can be

transported by deep convection to the UTLS and trapped within the anticyclonic circulation (e.g., Li et al., 2005; Fu et al., 2006; Park et al. 2009). This may account for the high CO over these two regions even though local emission is relatively weak. Over Indonesia, MLS roughly shows two high CO centers, one occurs when both convection and emission are strong (upper right corner) and the other exists when strong emission with weak convection is present (lower right corner).

The emission-convection-CO relationships simulated by the two models are quite similar to each other, reflecting their underlying identical meteorology and similar emission inventories. When compared with MLS observation, there is similarity over some regions such as southern Africa, northern Africa and Indonesia. Over other regions, the observed and simulated relationships are quite different. For example, both GMI and GEOS-Chem show two CO centers when convection is strong (CONV > 1) over South America, and they overestimate CO when convection is moderate (0.1 < CONV < 1). Over East Asia, both models overestimate CO when convection is weak or moderate, especially with weak emission (< 0.2 g/m^2/month). Over South Asia, both models show a high CO center when both convection and emission are weak (lower left corner), which is not seen in the MLS observation. The emission-convection-CO relationships at 147 hPa over different regions observed by MLS, and the comparisons between observation and model simulations are similar to those at 215 hPa, thus we will not discuss them in detail.

6 Conclusions

In this study, we evaluate the spatial distribution and temporal variation of CO in the upper troposphere and lower stratosphere (UTLS) during 2004–2012 simulated by two chemical transport models (GMI and GEOS-Chem) using the latest version (V4.2) of

Aura MLS data. The seasonal and monthly variations of CO, as well as the transport of CO in the UTLS (the "tape recorder") are compared between MLS observations and model simulations, over both global and regional scales. In addition, the relationships between emission, convection, and CO mixing ratio in the UTLS are investigated over different regions using MLS observations and model simulations.

In general, the simulated CO distribution from GMI is quite similar to that from GEOS-Chem at all levels. However, the CO peak values of GEOS-Chem are ~15-20% smaller than GMI at 215 hPa and 147 hPa over South America and Africa during DJF and SON, and ~20% larger than GMI at 100 hPa over South Asia during JJA. Compared with MLS observation, the locations of high CO centers at 215 hPa and 147 hPa are well simulated in GMI and GEOS-Chem, except over Africa. The UTLS transport of CO from East Asia across the Pacific to North America in MAM and JJA is ~~not well simulated~~shown ~~by~~ in the two models' simulations, but the CO concentrations are much lower than those observed by MLS~~, suggesting perhaps insufficient lofting of polluted continental air masses by warm conveyer belts~~. In addition, the magnitudes of simulated CO peaks are much smaller than MLS observation, with a maximum underestimation of ~40% at 215 hPa, 50–60% at 147 hPa, and ~70% at 100 hPa. For the vertical distribution of zonally averaged CO, the model simulations show more diffuse UT horizontal gradients, stronger vertical gradients below 100 hPa and weaker gradients above 100 hPa than observed by MLS, which may be due to the underestimated upward transport of CO. The two models successfully reproduce the seasonal shift of CO centers in the UT from DJF to JJA, but they fail to simulate a higher CO maximum in the southern subtropics during SON.

607 The high CO concentrations in the northern subtropics are largely underestimated in
608 the models from April to July, especially over South Asia and East Asia. By contrast, the
609 temporal variation of CO in the southern subtropics is well simulated by the models,
610 except that the magnitude is slightly smaller than observed. The high CO values in the
611 UT related to stronger CO emissions generated by drought-induced fires in Indonesia or
612 South America are well captured by GMI during ENSO periods. The semi-annual CO
613 peaks at 100 hPa are not well simulated by the two models, and the peak during MAM is
614 much weaker than the other peak during SON. In general, the observed and simulated CO
615 tape recorders show good agreement over the tropics and southern subtropics. The phase
616 shift and CO anomaly magnitude in the GMI simulation are more consistent with MLS
617 observation than those in the GEOS-Chem simulation. The models show that the location
618 of the tape head is near 200 hPa, which is in rough agreement with MLS data. Over the
619 northern subtropics, CO tape recorders simulated by the models show a 2-3 month time
620 lag between the same phases of CO peak anomaly, which may be caused by an
621 underestimation of vertical transport in the models.

622 On regional scales, the CO concentrations simulated by GMI are generally larger than
623 those from GEOS-Chem, with differences less than 10% at 215 hPa and 147 hPa. The
624 seasonal cycle of CO is similar between MLS and both models over South America,
625 southern Africa and Indonesia, although the magnitude greatly differs. Over three other
626 regions (northern Africa, East Asia, South Asia), the simulated seasonal variation of CO
627 is not consistent with MLS observation. At 100 hPa, GMI is smaller than GEOS-Chem
628 over all regions, especially from May to October. The underestimation of CO by the
629 models reaches its maximum at this level. Vertical CO profile comparisons show that the

models underestimate CO at all levels below (i.e., with pressures greater than) 50 hPa observable by MLS, with the magnitude of underestimation depending on region, altitude and season.

The relationships between emission, convection and UTLS CO vary with region. Over the tropics, UT CO generally increases with increasing surface emission in the presence of deep convection. When convection is relatively weak, UT CO is generally low and changes little with surface emission. The maximum CO concentration occurs when both convection and emission are strong. GMI and GEOS-Chem simulations generally show similar emission-convection-CO relationships compared with MLS observation at 215 hPa and 147 hPa, except the slope of CO contours have some differences. At 100 hPa, the emission-convection-CO relationships simulated by the two models are quite different from observations. On a regional scale, CO in the UT is generally high when emission and convection are strong, but distinct regional differences also exist, which may be associated with the relative importance of convection and advection in CO transport over different regions. In addition, convection in the tropics and mid-latitudes are fundamentally different, leading to differences in CO transport, and the relative mix of CO from anthropogenic emission, biomass burning, and in-situ production. The simulated emission-convection-CO relationships from GMI and GEOS-Chem are similar to observation over some regions such as southern Africa, northern Africa and Indonesia, but not all regions.

Overall, GMI and GEOS-Chem simulations of CO are similar given the same driving meteorology and very similar emission inventories. However, model simulations still show large discrepancies compared with MLS observations, especially in the lower

stratosphere, such as at 100 hPa. These discrepancies may be related to the convection parameterization, inaccurate emission inventories, and chemical production and loss rate of CO in the troposphere (e.g., Table 2). More efforts are needed to investigate these factors to improve model simulations in future studies.

Appendix A: Comparison of MLS Version 3 and Version 4 CO

Our preliminary comparisons of MLS V3 and V4 CO data have shown that the spatial distributions of CO in the UTLS are quite similar, except for some small differences in the magnitude. In general, CO concentration differences between these two versions are within 20%. The seasonal CO peak values of V4 are slightly larger than V3 at 215 hPa and 147 hPa, but become smaller than V3 at 100 hPa. The maximum differences is ~12–17% for different seasons.

The improvements of MLS V4 compared with V3 CO can be seen in the vertical distribution of zonal mean CO (Fig. A1) and the vertical CO profiles (Fig. A2). One improvement is that the cloud contamination is significantly reduced, the other is the more realistic CO gradient from 215 hPa to 100 hPa. In order to better illustrate the differences between different versions, we also add the CO measurements from the Atmospheric Chemistry Experiment - Fourier Transform Spectrometer (ACE-FTS) (Bernath et al., 2005). This instrument is on board the Canadian satellite SCISAT-1, operating between 750 and 4400 cm^{-1} with a high spectral-resolution (0.02 cm^{-1}) and using a solar occultation observation technique. ACE-FTS observations are used to derive volume mixing ratio profiles of over 30 atmospheric trace gases (Boone et al., 2005), measuring each spacecraft sunrise and sunset (~30 profiles per day compared to ~3500

for Aura MLS). It has been providing consistent measurements since February 2004. The atmospheric profiles provided by ACE-FTS range in altitude of ~5–110 km depending on the species, with a vertical resolution of ~3–4 km. The data used are ACE-FTS Level 2 Version 3.5 (V3.5) (Boone et al., 2013) with the same period as MLS data (August 2004 – December 2012).

The vertical distribution of zonal mean CO in the pressure-latitude cross-section and its seasonal variations as observed by MLS and ACE-FTS are shown in Figure A1. During boreal Winter (DJF), MLS V3 CO shows a decrease between 160 hPa and 130 hPa, which may be caused by cloud contamination. This abnormal gap does not exist in MLS V4 and ACE-FTS CO observation. Such improvement is also shown during MAM. In addition, the magnitude of high CO centers in MLS V4 is higher than that in MLS V3 and has better agreement with ACE-FTS measurement. The tropical average (30 °S–30 °N) of CO vertical profile in the UTLS and its seasonal variation as observed by MLS and ACE-FTS are shown in Figure A2. Compared with MLS V3 data, V4 CO is slightly more realistic in the CO gradient from 215 hPa to 100 hPa. For example, MLS V3 data show that CO decreases from 215 hPa to 147 hPa and then increases from 147 hPa to 100 hPa during DJF season, but V4 data show that it monotonically decreases from 215 hPa to 100 hPa, which is consistent with ACE-FTS CO observation. This improvement is also found in regional analysis (e.g., Indonesia). Furthermore, MLS V4 CO also shows better agreement with ACE-FTS CO than V3 CO during other seasons.

Acknowledgements

This research is supported by the NASA Aura Science Team~~AST~~ program. The study was performed at ~~NASA~~ the Jet Propulsion Laboratory (JPL), ~~at the~~ California Institute of Technology, under contract with NASA. The first author would like to thank Dr. William G. Read for help with the application of MLS averaging kernels to model simulations, and thank Dr. Susan E. Strahan and Dr. Stephen D. Steenrod for helpful advice on GMI model data analysis. We appreciate the helpful comments from two anonymous reviewers that led to significant improvements of this paper.

References

Alexander, B., Savarino, J., Lee, C. C. W., Park, R. J., Jacob, D. J., Thiemens, M. H., Li, Q. B., and Yantosca, R. M.: Sulfate formation in sea-salt aerosols: Constraints from oxygen isotopes, J. Geophys. Res., 110, D10307, doi:10.1029/2004JD005659, 2005.

Allen, D. J., Kasibhatla, P., Thompson, A. M., Rood, R. B., Doddridge, B. G., Pickering, K. E., Hudson, R. D., and Lin, S.: Transport-induced interannual variability of carbon monoxide determined using a chemistry and transport model, J. Geophys. Res., 101, 28655–28669, 1996.

Barkley, M., P. Palmer, L. Ganzeveld, A. Arneth, D. Hagberg, T. Karl, A. Guenther, F. Paulot, P. Wennberg, J. Mao, T. Kurosu, K. Chance, J.-F. Muller, I. De Smedt, M. Van Roozendael, D. Chen, Y. Wang, and R. Yantosca: Can a "state of the art" chemistry transport model simulate Amazonian tropospheric chemistry? , J. Geophys. Res., 116, D16302, doi:10.1029/2011JD015893, 2011.

Bernath, P. F., McElroy, C. T., Abrams, M. C., Boone, C. D., Butler, M., Camy-Peyret, C., Carleer, M., Clerbaux, C., Coheur, P.-F., Colin, R., DeCola, P., DeMazière, M.,

721 Drummond, J. R., Dufour, D., Evans,W. F. J., Fast, H., Fussen, D., Gilbert, K.,
722 Jennings, D. E., Llewellyn, E. J., Lowe, R. P., Mahieu, E., McConnell, J. C., McHugh,
723 M., McLeod, S. D., Michaud, R., Midwinter, C., Nassar, R., Nichitiu, F., Nowlan, C.,
724 Rinsland, C. P., Rochon, Y. J., Rowlands, N., Semeniuk, K., Simon, P., Skelton, R.,
725 Sloan, J. J., Soucy, M.-A., Strong, K., Tremblay, P., Turnbull, D., Walker, K.
726 A.,Walkty, I.,Wardle, D. A.,Wehrle, V., Zander, R., and Zou, J.: Atmospheric
727 Chemistry Experiment (ACE): Mission overview, Geophys. Res. Lett., 32, L15S01,
728 doi:10.1029/2005GL022386, 2005.
729 Bey, I., Aumont, B., and Toupance, G.: A modeling study of the nighttime radical
730 chemistry in the lower continental troposphere: 1. Development of a detailed chemical
731 mechanism including nighttime chemistry, J. Geophys. Res., 106(D9), 9959–9990,
732 doi:10.1029/2000JD900347, 2001a.
733 Bey, I., Jacob, D. J., Yantosca, R. M., Logan, J. A., Field, B. D., Fiore, A. M., Li, Q. B.,
734 Liu, H. G. Y., Mickley, L. J., and Schultz, M. G.: Global modeling of tropospheric
735 chemistry with assimilated meteorology: Model description and evaluation, J. Geophys.
736 Res., 106, 23073–23096, 2001b.
737 Bian, H., and Prather, M. J.: Fast-J2: Accurate Simulation of stratospheric photolysis in
738 global chemical models, J. Atmos. Chem., 41, 281–296, 2002.
739 Boone, C. D., Nassar, R., Walker, K. A., Rochon, Y., McLeod, S. D., Rinsland, C. P., and
740 Bernath, P. F.: Retrievals for the Atmospheric Chemistry Experiment
741 Fourier-Transform Spectrometer, Appl. Optics, 44, 7218–7231,
742 doi:10.1364/AO.44.007218, 2005.

743 Boone, C. D., Walker, K. A., and Bernath, P. F.: Version 3 Retrievals for the
744 Atmospheric Chemistry Experiment Fourier Transform Spectrometer (ACE-FTS), The
745 Atmospheric Chemistry Experiment ACE at 10: A Solar Occultation Anthology, A.
746 Deepak Publishing, Hampton, Virginia, USA, 103–127, 2013.
747 Brewer, A. W.: Evidence for a World Circulation Provided by the Measurements of
748 Helium and Water Vapour Distribution in the Stratosphere, Q. J. Roy. Meteor. Soc., 75,
749 351–363, 1949.
750 Daniel, J. S., and Solomon, S.: On the climate forcing of carbon monoxide, J. Geophys.
751 Res., 103, 13249–13260, 1998.
752 De Laat, A., Gloudemans, A., Aben, I., Krol, M., Meirink, J., van der Werf, G., and
753 Schrijver, H.: SCIAMACHY carbon monoxide total columns: statistical evaluation and
754 comparison with CTM results, J. Geophys. Res., 112, D12310,
755 doi:10.1029/2006JD008256, 2007.
756 Duncan, B. N., Strahan, S. E., Yoshida, Y., Steenrod, S. D., and Livesey, N.: Model study
757 of the cross-tropopause transport of biomass burning pollution, Atmos. Chem. Phys., 7,
758 3713–3736, doi:10.5194/acp-7-3713-2007, 2007.
759 Edwards, D. P., Emmons, L. K., Gille, J. C., Chu, A., Attie, J. L., Giglio, L., Wood, S. W.,
760 Haywood, J., Deeter, M. N., Massie, S. T., Ziskin, D. C., and Drummond, J. R.:
761 Satellite-observed pollution from Southern Hemisphere biomass burning, J. Geophys.
762 Res., 111, D14312, doi:10.1029/2005JD006655, 2006.
763 Fisher, J. A., Wilson, S. R., Zeng, G., Williams, J. E., Emmons, L. K., Langenfelds, R. L.,
764 Krummel, P. B., and Steele, L. P.: Seasonal changes in the tropospheric carbon
765 monoxide profile over the remote Southern Hemisphere evaluated using multi-model

766 simulations and aircraft observations, Atmos. Chem. Phys., 15, 3217-3239,
767 doi:10.5194/acp-15-3217-2015, 2015.
768 Fu, R., Hu, Y. L., Wright, J. S., Jiang, J. H., Dickinson, R. E., Chen, M. X., Filipiak, M.,
769 Read, W. G., Waters, J. W., and Wu, D. L.: Short circuit of water vapor and polluted
770 air to the global stratosphere by convective transport over the Tibetan Plateau, P. Natl.
771 Acad. Sci. USA, 103, 5664–5669, doi:10.1073/pnas.0601584103, 2006.
772 Gloudemans, A., Krol, M., Meirink, J., De Laat, A., Van der Werf, G., Schrijver, H., Van
773 den Broek, M., and Aben, I.: Evidence for long-range transport of carbon monoxide in
774 the Southern Hemisphere from SCIAMACHY observations, Geophys. Res. Lett., 33,
775 L16807, doi:10.1029/2006GL026804, 2006.
776 Gonzi, S., and Palmer, P. I.: Vertical transport of surface fire emissions observed from
777 space, J. Geophys. Res., 115, D02306, doi:10.1029/2009JD012053, 2010.
778 Guenther, A., Karl, T., Harley, P., Wiedinmyer, C., Palmer, P. I., and Geron, C.:
779 Estimates of global terrestrial isoprene emissions using MEGAN (Model of Emissions
780 of Gases and Aerosols from Nature), Atmos. Chem. Phys., 6, 3181–3210,
781 doi:10.5194/acp-6-3181-2006, 2006.
782 Heald, C. L., D. J. Jacob, D. B. A. Jones, P. I. Palmer, J. A. Logan, D. G. Streets, G. W.
783 Sachse, J. C. Gille, R. N. Hoffman, and T. Nehrkorn: Comparative inverse analysis of
784 satellite (MOPITT) and aircraft (TRACE-P) observations to estimate Asian sources of
785 carbon monoxide, J. Geophys. Res., 109, D23306, doi:10.1029/2004JD005185, 2004.
786 Huang, L., Fu, R., Jiang, J. H., Wright, J. S., and Luo, M.: Geographic and seasonal
787 distributions of CO transport pathways and their roles in determining CO centers in the

upper troposphere, Atmos. Chem. Phys., 12, 4683–4698, doi:10.5194/acp-12-4683-2012, 2012.

Huang, L., Fu, R., and Jiang, J. H.: Impacts of fire emissions and transport pathways on the interannual variation of CO in the tropical upper troposphere, Atmos. Chem. Phys., 14, 4087-4099, doi:10.5194/acp-14-4087-2014, 2014.

Hudman, R. C., et al.: Surface and lightning sources of nitrogen oxides over the United States: Magnitudes, chemical evolution, and outflow, J. Geophys. Res., 112, D12S05, doi:10.1029/2006JD007912, 2007

Jacob, D. J., Introduction to Atmospheric Chemistry, Princeton University Press, Princeton, New Jersey, USA, 1999.

Jiang, J. H., Livesey, N. J., Su, H., Neary, L., McConnell, J. C., and Richards, N. A. D.: Connecting surface emissions, convective uplifting, and long-range transport of carbon monoxide in the upper troposphere: New observations from the Aura Microwave Limb Sounder, Geophys Res Lett, 34, Doi 10.1029/2007gl030638, 2007.

Jiang, J. H., Su, H., Zhai, C., Massie, S. T., Schoeberl, M. R., Colarco, P. R., Platnick, S., Gu, Y., and Liou, K.-N.: Influence of convection and aerosol pollution on ice cloud particle effective radius, Atmos. Chem. Phys., 11, 457–463, doi: 10.5194/acp-11-457-2011, 2011.

Kiehl, J. T., Hack, J. J., Bonan, G. B., Boville, B. A., Williamson, D. L., and Rasch, P. J.: The National Center for Atmospheric Research Community Climate Model: CCM3, J. Clim., 11(6), 1131–1149, 1998.

Kopacz, M., D. J. Jacob, D. Henze, C. L. Heald, D. G. Streets, and Q. Zhang: Comparison of adjoint and analytical Bayesian inversion methods for constraining

811 Asian sources of carbon monoxide using satellite (MOPITT) measurements of CO
812 columns, J. Geophys. Res., 114, D04305, doi:10.1029/2007JD009264, 2009.
813 Kopacz, M., Jacob, D. J., Fisher, J. A., Logan, J. A., Zhang, L., Megretskaia, I. A.,
814 Yantosca, R. M., Singh, K., Henze, D. K., Burrows, J. P., Buchwitz, M., Khlystova, I.,
815 McMillan, W. W., Gille, J. C., Edwards, D. P., Eldering, A., Thouret, V., and Nedelec,
816 P.: Global estimates of CO sources with high resolution by adjoint inversion of
817 multiple satellite datasets (MOPITT, AIRS, SCIAMACHY, TES), Atmos. Chem.
818 Phys., 10, 855-876, doi:10.5194/acp-10-855-2010, 2010.
819 Li, Q. B., Jiang, J. H., Wu, D. L., Read, W. G., Livesey, N. J., Waters, J. W., Zhang, Y. S.,
820 Wang, B., Filipiak, M. J., Davis, C. P., Turquety, S., Wu, S. L., Park, R. J., Yantosca,
821 R. M., and Jacob, D. J.: Convective outflow of South Asian pollution: A global CTM
822 simulation compared with EOS MLS observations, Geophys. Res. Lett., 32, L14826,
823 doi:10.1029/2005GL022762, 2005.
824 Liu, C. T., Zipser, E., Garrett, T., Jiang, J. H., and Su, H.: How do the water vapor and
825 carbon monoxide “tape recorders” start near the tropical tropopause?, Geophys Res
826 Lett, 34, doi: 10.1029/2006gl029234, 2007.
827 Liu, J., Logan, J. A., Jones, D. B. A., Livesey, N. J., Megretskaia, I., Carouge, C., and
828 Nedelec, P.: Analysis of CO in the tropical troposphere using Aura satellite data and
829 the GEOS-Chem model: insights into transport characteristics of the GEOS
830 meteorological products, Atmos Chem Phys, 10, 12207-12232, DOI
831 10.5194/acp-10-12207-2010, 2010.
832 Liu, J., Logan, J. A., Murray, L. T., Pumphrey, H. C., Schwartz, M. J., and
833 Megretskaia, I. A.: Transport analysis and source attribution of seasonal and

834 interannual variability of CO in the tropical upper troposphere and lower stratosphere,
835 Atmos. Chem. Phys., 13, 129–146, doi: 10.5194/acp-13-129-2013, 2013.
836 Livesey, N. J., Filipiak, M. J., Froidevaux, L., Read, W. G., Lambert, A., Santee, M. L.,
837 Jiang, J. H., Pumphrey, H. C., Waters, J. W., Cofield, R. E., Cuddy, D. T., Daffer, W.
838 H., Drouin, B. J., Fuller, R. A., Jarnot, R. F., Jiang, Y. B., Knosp, B. W., Li, Q. B.,
839 Perun, V. S., Schwartz, M. J., Snyder, W. V., Stek, P. C., Thurstans, R. P., Wagner, P.
840 A., Avery, M., Browell, E. V., Cammas, J. P., Christensen, L. E., Diskin, G. S., Gao, R.
841 S., Jost, H. J., Loewenstein, M., Lopez, J. D., Nedelec, P., Osterman, G. B., Sachse, G.
842 W., and Webster, C. R.: Validation of Aura Microwave Limb Sounder O-3 and CO
843 observations in the upper troposphere and lower stratosphere, J Geophys Res-Atmos,
844 113, Doi 10.1029/2007jd008805, 2008.
845 Livesey, N. J., Read, W. G., Froidevaux, L., Lambert, A., Manney, G. L.: EOS MLS
846 version 3.3 Level 2 data quality and description document, Jet Propulsion Laboratory,
847 California Institute of Technology, Pasadena, CA, 2011.
848 Livesey, N. J., Logan, J. A., Santee, M. L., Waters, J. W., Doherty, R. M., Read, W. G.,
849 Froidevaux, L., and Jiang, J. H.: Interrelated variations of O3, CO and deep convection
850 in the tropical/subtropical upper troposphere observed by the Aura Microwave Limb
851 Sounder (MLS) during 2004–2011, Atmos. Chem. Phys., 13, 579-598,
852 doi:10.5194/acp-13-579-2013, 2013.
853 Livesey, N. J., Read, W. G., Wagner, P. A., Froidevaux, L., Lambert, A., Manney, G. L.,
854 Millán, L., Pumphrey, H. C., Santee, M. L., Schwartz, M. J., Wang, S., Fuller, R. A.,
855 Jarnot, R. F., Knosp, B. W., and Martinez, E.: EOS MLS Version 4.2x Level 2 data

quality and description document, Jet Propulsion Laboratory, California Institute of Technology, Pasadena, CA, 2015.

Logan, J. A., Prather, M. J., Wofsy, S. C., and McElroy, M. B.: Tropospheric chemistry: A global perspective, J. Geophys. Res., 86, 7210–7254, 1981.

Mote, P. W., Rosenlof, K. H., Holton, J. R., Harwood, R. S., and Waters, J. W.: Seasonal variations of water vapor in the tropical lower stratosphere, Geophys. Res. Lett., 22, 1093–1096, 1995.

Murray, L. T., Logan, J. A., and Jacob, D. J.: Interannual variability in tropical tropospheric ozone and OH: the role of lightning, J. Geophys. Res., 118, 11468–11480, doi:10.1002/jgrd.50857, 2013.

Naik, V., Voulgarakis, A., Fiore, A. M., Horowitz, L. W., Lamarque, J.-F., Lin, M., Prather, M. J., Young, P. J., Bergmann, D., Cameron-Smith, P. J., Cionni, I., Collins, W. J., Dalsøren, S. B., Doherty, R., Eyring, V., Faluvegi, G., Folberth, G. A., Josse, B., Lee, Y. H., MacKenzie, I. A., Nagashima, T., van Noije, T. P. C., Plummer, D. A., Righi, M., Rumbold, S. T., Skeie, R., Shindell, D. T., Stevenson, D. S., Strode, S., Sudo, K., Szopa, S., and Zeng, G.: Preindustrial to present-day changes in tropospheric hydroxyl radical and methane lifetime from the Atmospheric Chemistry and Climate Model Intercomparison Project (ACCMIP), Atmos. Chem. Phys., 13, 5277-5298, doi:10.5194/acp-13-5277-2013, 2013.

Park, M., Randel, W. J., Emmons, L. K., and Livesey, N. J.: Transport pathways of carbon monoxide in the Asian summer monsoon diagnosed from Model of Ozone and Related Tracers (MOZART), J. Geophys. Res., 114, D08303, doi:10.1029/2008JD010621, 2009.

879 Park, R. J., Jacob, D. J., Chin, M., and Martin, R. V.: Sources of carbonaceous aerosols
880 over the United States and implications for natural visibility, J. Geophys. Res., 108,
881 4355, doi:10.1029/2002JD003190, 2003.
882 Randel, W. J. and Jensen, E. J.: Physical processes in the tropical tropopause layer and
883 their roles in a changing climate, Nat. Geosci., 6, 169–176, doi:10.1038/ngeo1733,
884 2013.
885 Randel, W. J., Park, M., Emmons, L., Kinnison, D., Bernath, P., Walker, K. A., Boone,
886 C., and Pumphrey, H.: Asian monsoon transport of pollution to the stratosphere,
887 Science, 328, 611–613, 2010.
888
889 Ricaud, P., Barret, B., Attié, J.-L., Motte, E., Le Flochmoën, E., Teyssèdre, H., Peuch,
890 V.-H., Livesey, N., Lambert, A., and Pommereau, J.-P.: Impact of land convection on
891 troposphere-stratosphere exchange in the tropics, Atmos. Chem. Phys., 7, 5639–5657,
892 doi:10.5194/acp-7-5639-2007, 2007.
893 Rienecker, M. M., Suarez, M. J., Gelaro, R., Todling, R., Bacmeister, J., Liu, E.,
894 Bosilovich, M. G., Schubert, S. D., Takacs, L., Kim, G.-K., Bloom, S., Chen, J.,
895 Collins, D., Conaty, A., da Silva, A., Gu, W., Joiner, J., Koster, R. D., Lucchesi, R.,
896 Molod, A., Owens, T., Pawson, S., Pegion, P., Redder, C. R., Reichle, R., Robertson, F.
897 R., Ruddick, A. G., Sienkiewicz, M., and Woollen, J.: MERRA: NASA's Modern-Era
898 Retrospective Analysis for Research and Applications, J. Climate, 24, 3624–3648,
899 doi:10.1175/JCLI-D-11-00015.1, 2011.
900 Rotman, D. A., Tannahill J. R., Kinnison D. E., Connell, P. S., Bergmann, D., Proctor, D.,
901 Rodriguez, J. M., Lin, S. J., Rood, R. B., Prather, M. J., Rasch, P. J., Considine, D. B.,

902 Ramaroson, R., and Kawa, S. R.: Global Modeling Initiative assessment model: Model
903 description, integration, and testing of the transport shell, J. Geophys. Res., 106(D2),
904 1669–1691, doi:10.1029/2000JD900463, 2001.
905 Schoeberl, M. R., Duncan, B. N., Douglass, A. R., Waters, J., Livesey, N., Read, W., and
906 Filipiak, M.: The carbon monoxide tape recorder, Geophys. Res. Lett., 33, doi:
907 10.1029/2006gl026178, 2006.
908 Schultz, M., Rast, S., van het Bolscher, M., Pulles, T., Brand, R., Pereira, J., Mota, B.,
909 Spessa, A., Dalsøren, S., van Nojie, T., and Szopa, S.: Emission data sets and
910 methodologies for estimating emissions, RETRO project report D1-6, Hamburg,
911 available at: http://retro.enes.org/reports/D1-6_final.pdf, 26 February 2007.
912 Shindell, D., Faluvegi, G., Stevenson, D., Krol, M., Emmons, L., Lamarque, J.-F., Petron,
913 G., Dentener, F., Ellingsen, K., Schultz, M., Wild, O., Amann, M., Atherton, C. S.,
914 Bergmann, D. J., Bey, I., Butler, T., Cofala, J., Collins, W. J., Derwent, R. G., Doherty,
915 R. M.,Drevet, J., Eskes, H. J., Fiore, A. M., Gauss, M., Hauglustaine, D. A., Horowitz,
916 L. W., Isaksen, I. S. A., Lawrence, M. G., Montanaro, V., Müller, J.-F., Pitari, G.,
917 Prather, M. J., Pyle, J. A., Rast, S., Rodriguez, J. M., Sanderson, M. G., Savage, N. H.,
918 Strahan, S. E., Sudo, K., Szopa, S., Unger, N., van Noije, T. P. C., and Zeng, G.:
919 Multimodel simulations of carbon monoxide: Comparison with observations and
920 projected near-future changes, J. Geophys. Res., 111, D19306,
921 doi:10.1029/2006JD007100, 2006.
922 van der Werf, G. R., Randerson, J. T., Giglio, L., Collatz, G., Mu, M., Kasibhatla, P. S.,
923 Morton, D. C., DeFries, R., Jin, Y., and van Leeuwen, T. T.: Global fire emissions and

924 the contribution of deforestation, savanna, forest, agricultural, and peat fires (1997–
925 2009), Atmos. Chem. Phys, 10, 11,707–711,735, 2010.
926 van Donkelaar, A., Martin, R. V., Leaitch, W. R., Macdonald, A. M., Walker, T. W.,
927 Streets, D. G., Zhang, Q., Dunlea, E. J., Jimenez, J. L., Dibb, J. E., Huey, L. G., Weber,
928 R., and Andreae, M. O.: Analysis of aircraft and satellite measurements from the
929 Intercontinental Chemical Transport Experiment (INTEX-B) to quantify long-range
930 transport of East Asian sulfur to Canada, Atmos. Chem. Phys., 8, 2999-3014,
931 doi:10.5194/acp-8-2999-2008, 2008.
932 Waters, J.W., Froidevaux, L., Harwood, R. S., Jarnot, R. F., Pickett, H. M., Read, W. G.,
933 Siegel, P. H., Cofield, R. E., Filipiak, M. J., Flower, D. A., Holden, J. R., Lau, G. K.,
934 Livesey, N. J., Manney, G. L., Pumphrey, H. C., Santee, M. L., Wu, D. L., Cuddy, D.
935 T., Lay, R. R., Loo, M. S., Perun., V. S., Schwartz, M. J., Stek, P. C., Thurstans, R. P.,
936 Chandra, K. M., Chavez, M. C., Chen, G., Boyles, M. A., Chudasama, B. V., Dodge,
937 R., Fuller, R. A., Girard, M. A., Jiang, J. H., Jiang, Y., Knosp, B. W., LaBelle, R. C.,
938 Lam, J. C., Lee, K. A., Miller, D., Oswald, J. E., Patel, N. C., Pukala, D. M., Quintero,
939 O., Scaff, D. M., Snyder, W. V., Tope, M. C.,Wagner, P. A., andWalch, M. J.: The
940 Earth Observing System Microwave Limb Sounder (EOS MLS) on the Aura satellite,
941 IEEE Trans. Geosci. Remote Sens., 44, 1075–1092, 2006.
942 Wild, O., Zhu, X., and Prather, M.: Fast-J: Accurate simulation of in- and below- cloud
943 photolysis in tropospheric chemical models, J. Atmos. Chem., 37, 245–282, 2000.
944 Wu, D. L., Jiang, J. H., Read, W. G., Austin, R. T., David, C. P., Lambert, A., Stephens,
945 G. L., Vane, D. G., and Waters, J. W.: Validation of Aura MLS cloud Ice Water

946 Content (IWC) measurements, J. Geophys. Res., 113, D15S10,
947 doi:10.1029/2007LD008931, 2008.
948 Wu, S., L. J. Mickley, D. J. Jacob, J. A. Logan, R. M. Yantosca, and D. Rind: Why are
949 there large differences between models in global budgets of tropospheric ozone? J.
950 Geophys. Res., 112, D05302, doi:10.1029/2006JD007801, 2007.
951 Xiao, Y., J. A. Logan, D. J. Jacob, R. C. Hudman, R. Yantosca, and D. R. Blake: Global
952 budget of ethane and regional constraints on U.S. sources, J. Geophys. Res., 113,
953 D21306, doi:10.1029/2007JD009415, 2008.
954 Yevich, R., and Logan, J. A.: An assessment of biofuel use and burning of agricultural
955 waste in the developing world, Global Biogeochem. Cycles, 17, 1095,
956 doi:10.1029/2002GB001952, 2003.
957 Zeng, G., Williams, J. E., Fisher, J. A., Emmons, L. K., Jones, N. B., Morgenstern, O.,
958 Robinson, J., Smale, D., Paton-Walsh, C., and Griffith, D. W. T.: Multi-model
959 simulation of CO and HCHO in the Southern Hemisphere: comparison with
960 observations and impact of biogenic emissions, Atmos. Chem. Phys., 15, 7217-7245,
961 doi:10.5194/acp-15-7217-2015, 2015.
962 Zhang, G. J., and McFarlane, N. A.: Sensitivity of climate simulations to the
963 parameterization of cumulus convection in the Canadian Climate Centre general
964 circulation model, Atmos. Ocean., 33, 407–446, 1995.
965 Zhang, Q., Streets, D. G., Carmichael, G. R., He, K. B., Huo, H., Kannari, A., Klimont,
966 Z., Park, I. S., Reddy, S., Fu, J. S., Chen, D., Duan, L., Lei, Y., Wang, L. T., and Yao,
967 Z. L.: Asian emissions in 2006 for the NASA INTEX-B mission, Atmos. Chem. Phys.,
968 9, 5131-5153, doi:10.5194/acp-9-5131-2009, 2009.

Table Captions

Table 1. Differences between GMI model and GEOS-Chem model run.

Table 2~~1~~. Annual mean and interannual standard deviation of CO budgets (biofuel and fossil fuel emissions, biomass burning emissions, tropospheric chemical production, tropospheric methane oxidation, loss with tropospheric OH, and net transport from troposphere to stratosphere) for GMI and GEOS-Chem during 2004 – 2012 (units in Tmol/year).

Table 3~~2~~. Statistical comparison of model-simulated and MLS-observed (V4) CO at (a) 215 hPa, (b) 147 hPa, and (c) 100 hPa during each season.

Figure Captions

Fig. 1. Seasonal mean (DJF, MAM, JJA, and SON) distribution of CO mixing ratio at 215 hPa for December 2004 – November 2012 from: (top row) MLS V4 data; (middle row) GMI model simulation with MLS averaging kernels (AKs) applied; (bottom row) GEOS-Chem model simulation with MLS AKs applied.

Fig. 2. As in Fig. 1, but for CO mixing ratio at 147 hPa.

Fig. 3. As in Fig. 1, but for CO mixing ratio at 100 hPa.

Fig. 4. Vertical/latitudinal distribution of zonal mean CO mixing ratio during different seasons (DJF, MAM, JJA, and SON) from: (top row) MLS V4 data; (middle row) GMI model simulation with MLS AKs applied; (bottom row) GEOS-Chem model simulation with MLS AKs applied.

Fig. 5. Monthly variation of zonal mean CO mixing ratio at 215 hPa for August 2004 – December 2012 from: (top row) MLS V4 data; (middle row) GMI model simulation with MLS AKs applied; (bottom row) GEOS-Chem model simulation with MLS AKs applied.

Fig. 6. As in Fig. 5, but for CO mixing ratio at 100 hPa.

Fig. 7. Monthly variation of meridional mean (15 °S–15 °N) CO mixing ratio at 215 hPa for August 2004 – December 2012 from: (left) MLS V4 data; (middle) GMI model simulation with MLS AKs applied; (right) GEOS-Chem model simulation with MLS AKs applied.

Fig. 8. As in Fig. 7, but for CO mixing ratio at 100 hPa.

Fig. 9. Temporal variation of monthly mean CO deviations, zonally averaged over the tropics (15 °S–15 °N), vertically from 200 hPa to 50 hPa for August 2004 – December 2012 from (top row) MLS V4 data; (middle row) GMI model simulation with MLS AKs applied; (bottom row) GEOS-Chem model simulation with MLS AKs applied. An 8-year mean (2005–2012) was subtracted from the monthly mean time series at each level for MLS data and the two models' simulations.

Fig. 10. As in Fig. 9, but over the northern subtropics (10 °–30 °N).

Fig. 11. As in Fig. 9, but over the southern subtropics (10 °–30 °S).

Fig. 12. Climatological (8-year) monthly mean of CO mixing ratio at 215 hPa from MLS V4 data (black line), GMI model simulation with MLS AKs applied (red line), and GEOS-Chem model simulation with MLS AKs applied (blue line) over the selected six regions: (a) South America, (b) Southern Africa, (c) Northern Africa, (d) East Asia, (e) South Asia, and (f) Indonesia. The error bars indicate ±1 interannual standard deviation of the monthly mean CO from MLS _ –observation and model simulations~~V4 data~~.

Fig. 13. As in Fig. 12, but for CO mixing ratio at 100 hPa.

Fig. 14. Climatological (8-year) seasonal mean vertical profile of CO mixing ratio from MLS V4 data (black line), GMI model simulation with MLS AKs applied (red line), and GEOS-Chem model simulation with MLS AKs applied (blue line) over the selected six regions: (top row) South America, (second row from top) Southern Africa, (third row from top) Northern Africa, (fourth row from top) East Asia, (fifth row from top) South Asia, and (bottom row) Indonesia.

Fig. 15. Climatological monthly mean of surface CO emission from GMI model (red line), ice water content (blue line) and CO mixing ratio (black line) at 215 hPa (left column), 147 hPa (middle column), and 100 hPa (left column) from MLS observation over six regions: (top row) South America, (second row from top) Southern Africa, (third row from top) Northern Africa, (fourth row from top) East Asia, (fifth row from top) South Asia, and (bottom row) Indonesia. Each variable is normalized for comparison.

Fig. 16. Contour plots of normalized CO mixing ratio at 215 hPa (top row) and 147 hPa (bottom row) over the tropics (30°S–30°N) from MLS observation (left column), GMI model simulation (middle column), and GEOS-Chem model simulation (left column) binned according to the surface CO emission (x-axis) and convective index (y-axis) at the same pressure level. See text for more details.

Fig. 17. Contour plots of normalized CO mixing ratio at 215 hPa over six regions: (top row) South America, (second row from top) Southern Africa, (third row from top) Northern Africa, (fourth row from top) East Asia, (fifth row from top) South Asia, and (bottom row) Indonesia, from MLS observation (left column), GMI model simulation (middle column), and GEOS-Chem model simulation (left column) binned according to

the surface CO emission (x-axis) and convective index (y-axis) at the same pressure level. See text for more details.

Fig. A1. Vertical distribution of zonal mean CO mixing ratio in the pressure-latitude cross-section during different seasons (DJF, MAM, JJA, and SON) from: (top row) MLS Version 3 CO data; (middle row) MLS Version 4 CO data; (bottom row) ACE-FTS CO data with MLS averaging kernels (AKs) applied.

Fig. A2. Climatological (8-year) seasonal mean vertical profile of CO mixing ratio from MLS Version 4 CO data (black line), MLS Version 3 CO data (gray line), and ACE-FTS CO data with MLS AKs applied (red line) over the tropics (30 °S–30 °N).

Tables

Table 1. Differences between GMI model and GEOS-Chem model run.

	GMI	GEOS-Chem
Spin-up period	1990-1994	January 2003 – April 2004
Vertical resolution	72 levels (~38 levels in the tropical troposphere)	47 levels (~38 levels in the tropical troposphere)
Number of species	124	155
Number of chemical reactions	320	292
Number of photolytic reactions	81	64
chemistry mechanism	combined stratosphere/troposphere chemical mechanism	fully resolved in the troposphere, a linearized scheme applied in the stratosphere
Convective Parameterization	NCAR convection scheme	Relaxed Arakawa-Schubert scheme

Table 2~~1~~. Annual mean and interannual standard deviation of CO budgets (biofuel and fossil fuel emissions, biomass burning emissions, tropospheric chemical production,

Formatted: Font: 12 pt, Bold
Formatted: Font: 12 pt
Formatted: Font: 12 pt
Formatted Table
Formatted: Font: 12 pt
Formatted: Font: 12 pt
Formatted: Font: 12 pt
Formatted: Font: 12 pt
Formatted: Font: 12 pt
Formatted: Font: 12 pt
Formatted: Font: 12 pt
Formatted: Font: 12 pt

tropospheric methane oxidation, loss with tropospheric OH, and net transport from troposphere to stratosphere) for GMI and GEOS-Chem during 2004 – 2012 (units in Tmol/year).

Model	GMI	GEOS-Chem
biofuel + fossil fuel	20.6 ±0.16	19.6 ±0.29
biomass burning	11.9 ±1.9	11.9 ±2.0
tropospheric chemical production	42.3 ±0.92	59.1 ±0.77
~~tropospheric CH4 oxidation~~ *source from methane oxidation*	30.3 ±0.95	35.2 ±0.42
loss with tropospheric OH	77.7 ±2.1	89.1 ±2.4
net transport to stratosphere	1.37 ±0.49	1.50 ±0.47

Table ~~2~~3. Statistical comparison of model-simulated and MLS-observed (V4) CO at (a) 215 hPa, (b) 147 hPa, and (c) 100 hPa during each season.

Formatted Table
Formatted: Left
Formatted: Left
Formatted: Left
Formatted: Left
Formatted: Font: Italic
Formatted: Left
Formatted: Left
Formatted: Justified, Line spacing: Double

Level	Season	Correlation			Model Biases (%)								
					Maxinimum difference(%)			Miniaximum difference(%)			Mean difference (%)		
		GMI vs V4	GEOS vs V4	GMI vs GEOS	GMI-V4	GEOS-V4	GEOS - GMI	GMI-V4	GEOS-V4	GEOS - GMI	GMI-V4	GEOS-V4	GEOS - GMI
(a) 215 hPa	DJF	0.89	0.90	0.990	-39.0	-40.8	-21.4	30.7	14.5	3.2	-10.5	-16.6	-6.8
	MAM	0.90	0.90	0.995	-36.6	-37.9	-12.1	7.50	4.1	4.1	-20.0	-22.1	-2.7
	JJA	0.83	0.85	0.993	-40.3	-39.9	-6.8	13.7	9.9	8.9	-20.2	-19.5	0.8
	SON	0.85	0.82	0.983	-43.5	-47.9	-19.9	44.3	45.1	4.3	-11.1	-14.5	-3.8
(b) 147 hPa	DJF	0.92	0.93	0.996	-61.7	-60.0	-17.4	6.4	-2.1	5.6	-27.5	-29.1	-2.2
	MAM	0.96	0.95	0.998	-59.7	-59.2	-7.0	-6.6	-5.5	6.5	-32.4	-31.5	1.3
	JJA	0.96	0.97	0.997	-53.8	-52.0	-1.9	-4.4	-5.6	15.6	-31.3	-27.8	5.2
	SON	0.96	0.96	0.996	-50.0	-47.9	-13.7	5.0	6.2	10.3	-25.2	-24.1	1.4
(c) 100 hPa	DJF	0.93	0.94	0.999	-70.2	-68.4	-3.2	-21.9	-21.9	8.4	-46.1	-43.9	4.0
	MAM	0.97	0.97	0.999	-64.1	-63.0	1.0	-29.8	-27.1	10.0	-47.8	-44.8	5.6
	JJA	0.92	0.93	0.998	-67.9	-66.4	1.4	-23.7	-18.6	20.1	-47.4	-42.8	8.7
	SON	0.97	0.97	0.997	-61.7	-60.0	-0.6	-22.0	-18.0	14.6	-44.7	-40.6	7.5

Formatted Table

Figures

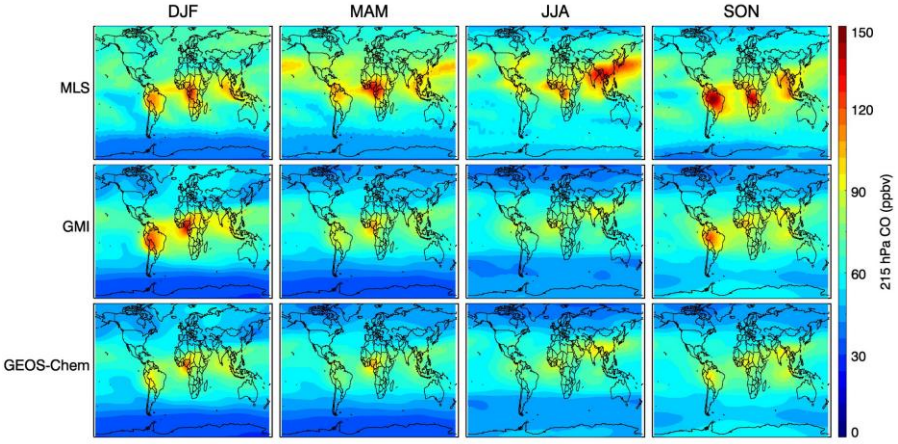

Fig. 1. Seasonal mean (DJF, MAM, JJA, and SON) distribution of CO mixing ratio at 215 hPa for December 2004 – November 2012 from: (top row) MLS V4 data; (middle row) GMI model simulation with MLS averaging kernels (AKs) applied; (bottom row) GEOS-Chem model simulation with MLS AKs applied.

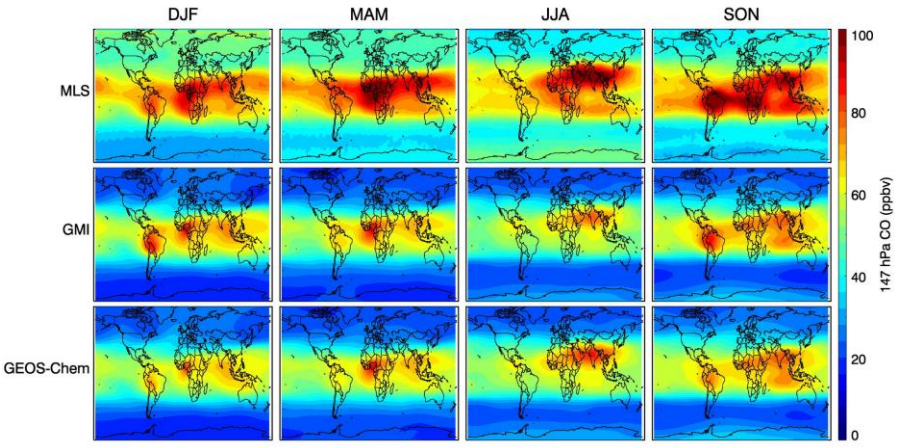

Fig. 2. As in Fig. 1, but for CO mixing ratio at 147 hPa.

1070

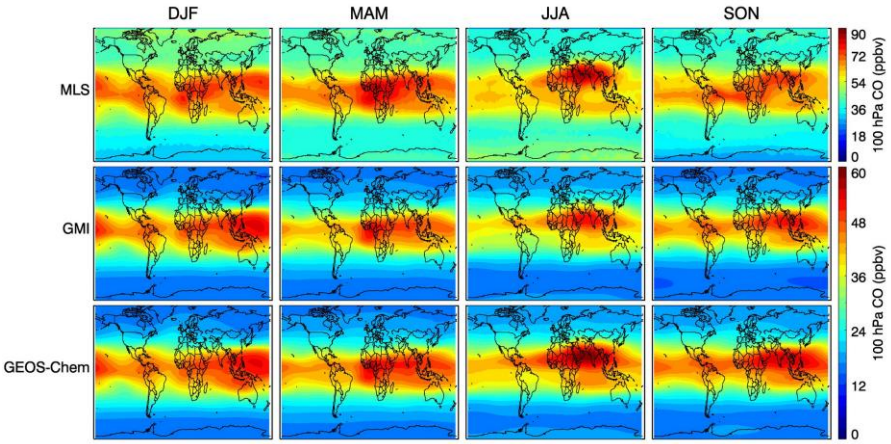

1071

1072 **Fig. 3.** As in Fig. 1, but for CO mixing ratio at 100 hPa.

1073

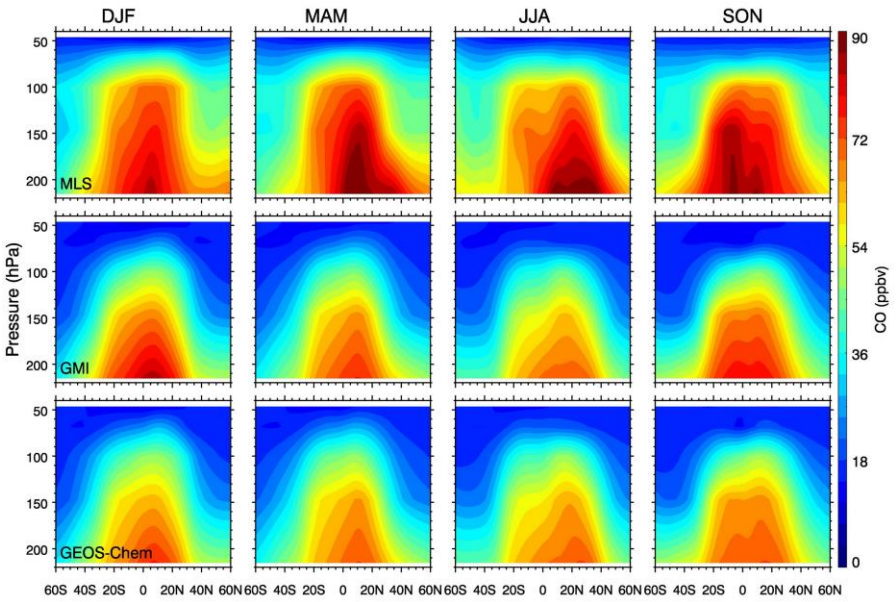

Fig. 4. Vertical/latitudinal distribution of zonal mean CO mixing ratio during different seasons (DJF, MAM, JJA, and SON) from: (top row) MLS V4 data; (middle row) GMI model simulation with MLS AKs applied; (bottom row) GEOS-Chem model simulation with MLS AKs applied.

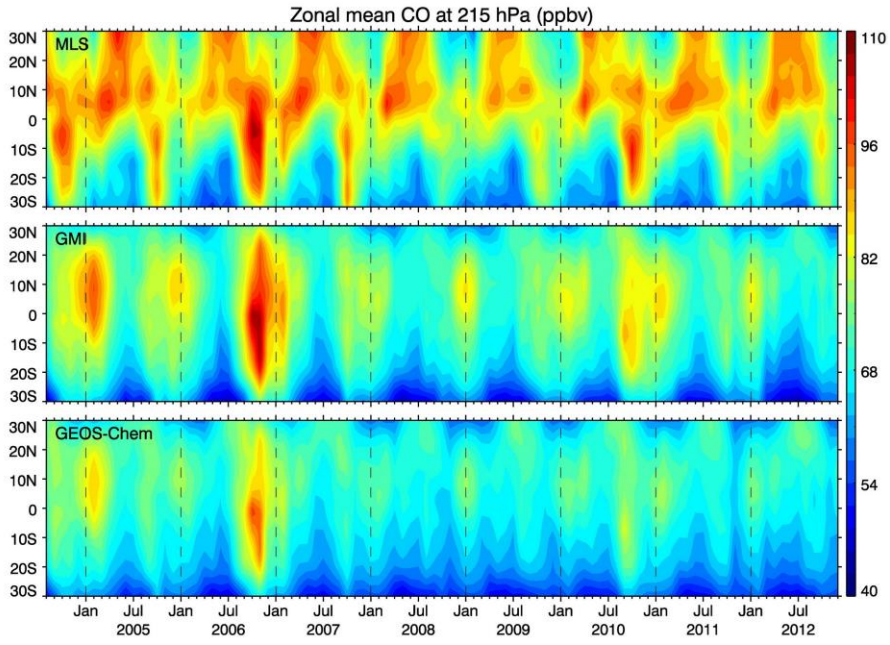

Fig. 5. Monthly variation of zonal mean CO mixing ratio at 215 hPa for August 2004 – December 2012 from: (top row) MLS V4 data; (middle row) GMI model simulation with MLS AKs applied; (bottom row) GEOS-Chem model simulation with MLS AKs applied.

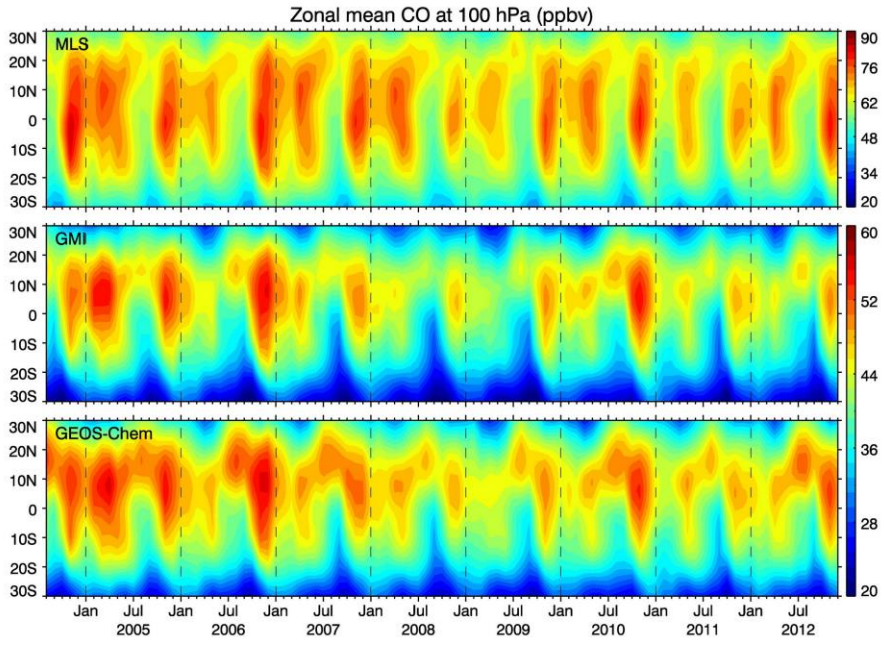

Fig. 6. As in Fig. 5, but for CO mixing ratio at 100 hPa.

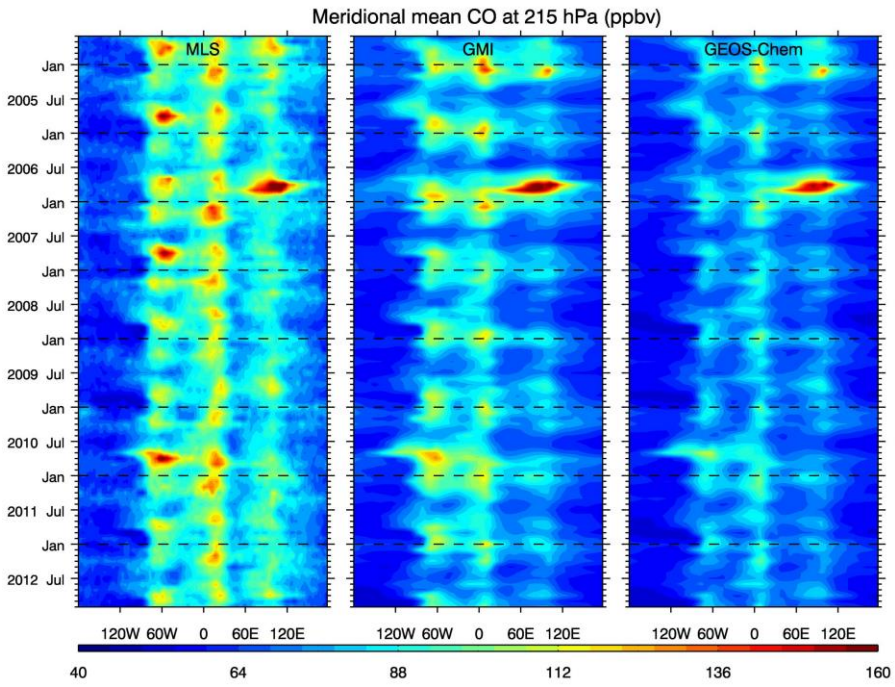

1087

1088 **Fig. 7.** Monthly variation of meridional mean (15°S–15°N) CO mixing ratio at 215 hPa
1089 for August 2004 – December 2012 from: (left) MLS V4 data; (middle) GMI model
1090 simulation with MLS AKs applied; (right) GEOS-Chem model simulation with MLS
1091 AKs applied.

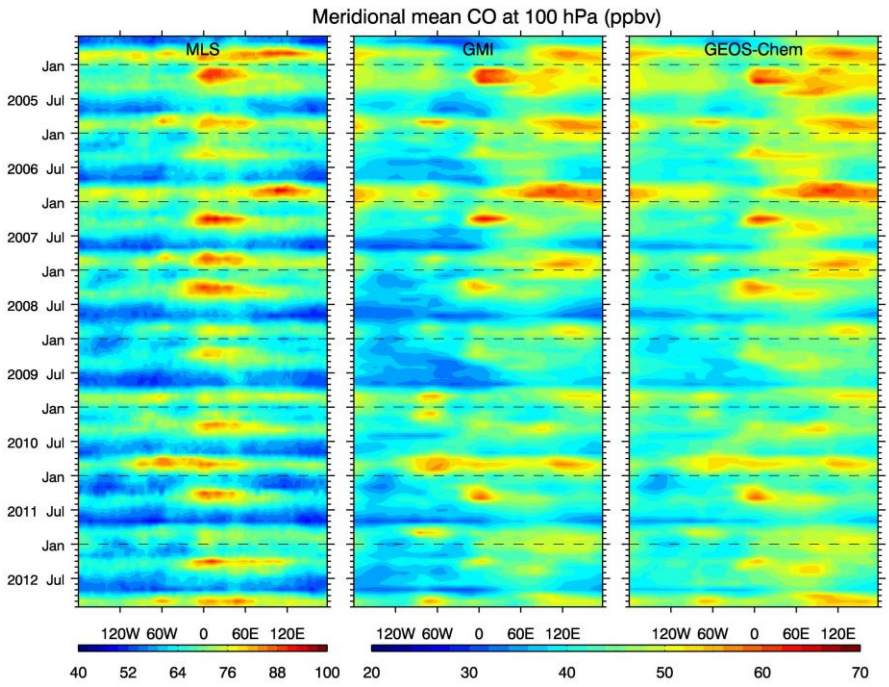

Fig. 8. As in Fig. 7, but for CO mixing ratio at 100 hPa.

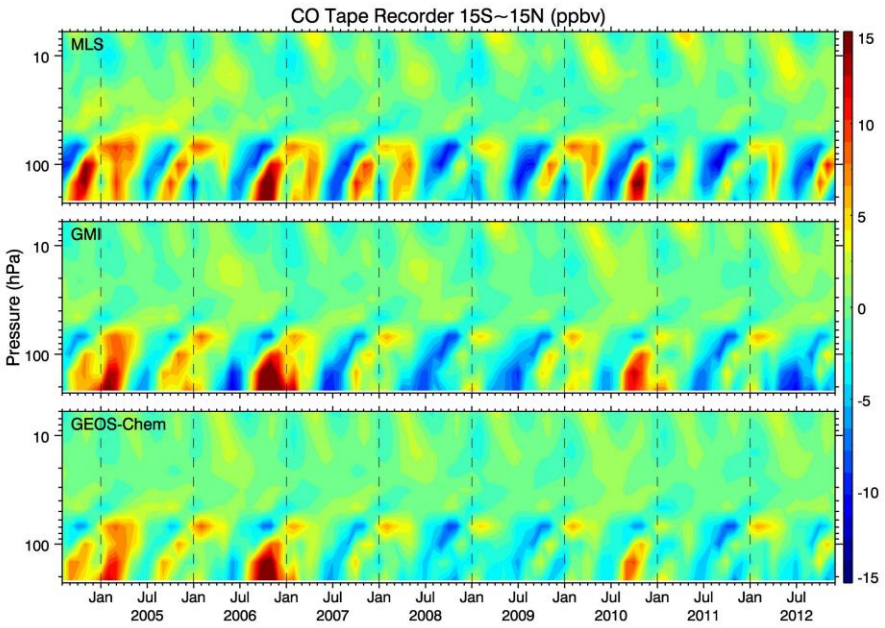

Fig. 9. Temporal variation of monthly mean CO deviations, zonally averaged over the tropics (15°S–15°N), vertically from 200 hPa to 50 hPa for August 2004 – December 2012 from (top row) MLS V4 data; (middle row) GMI model simulation with MLS AKs applied; (bottom row) GEOS-Chem model simulation with MLS AKs applied. An 8-year mean (2005–2012) was subtracted from the monthly mean time series at each level for MLS data and the two models' simulations.

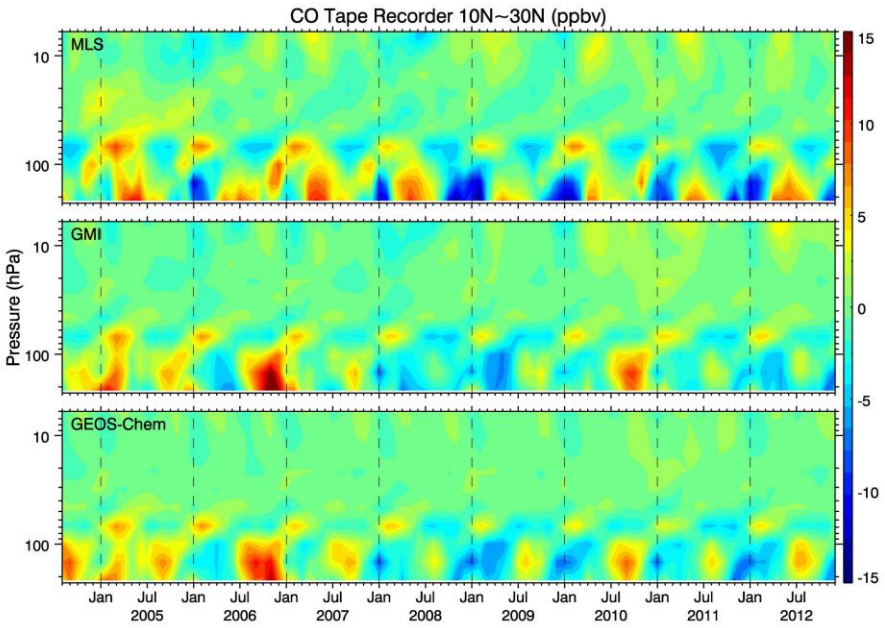

Fig. 10. As in Fig. 9, but over the northern subtropics (10 °–30 °N).

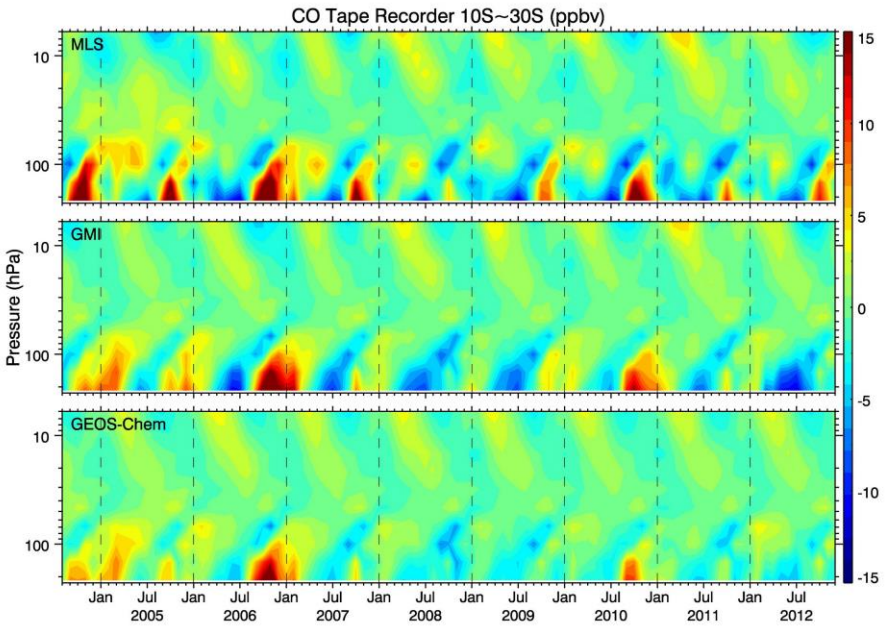

Fig. 11. As in Fig. 9, but over the southern subtropics (10 °–30 °S).

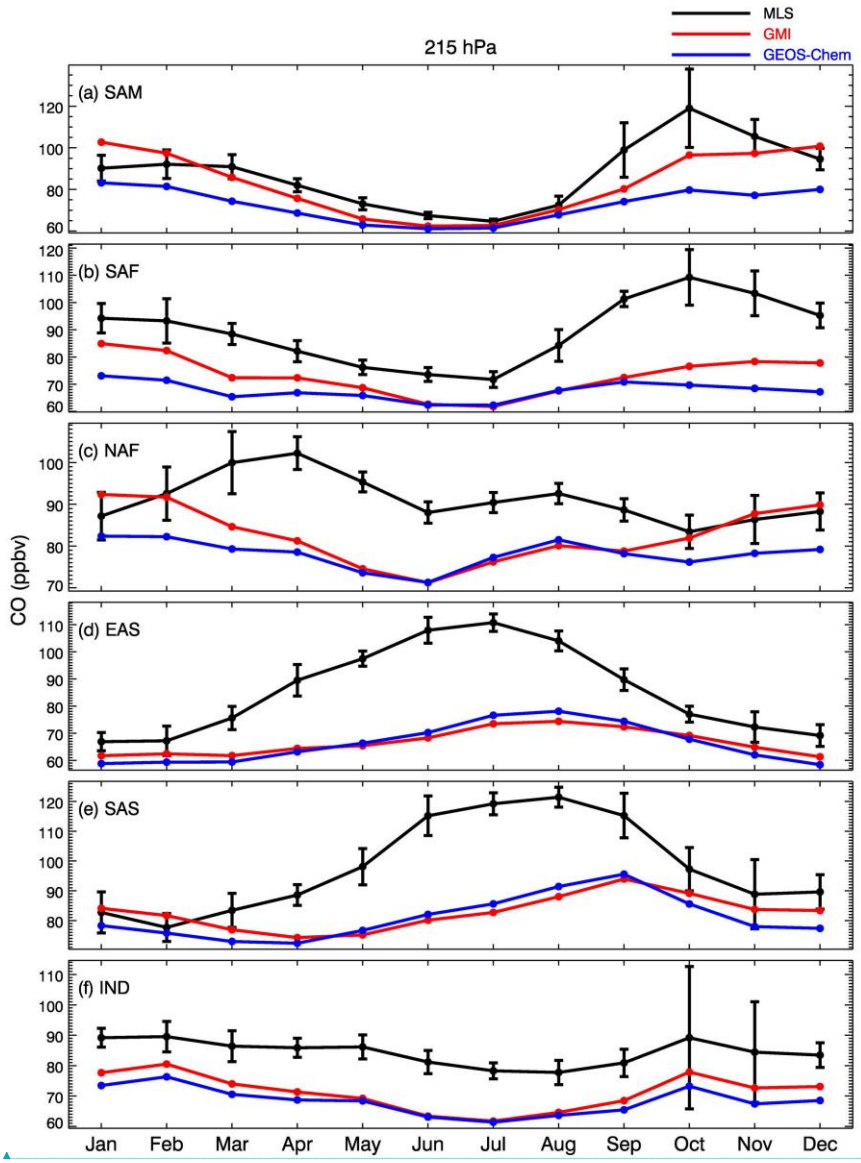

1107

Formatted: Font: 12 pt

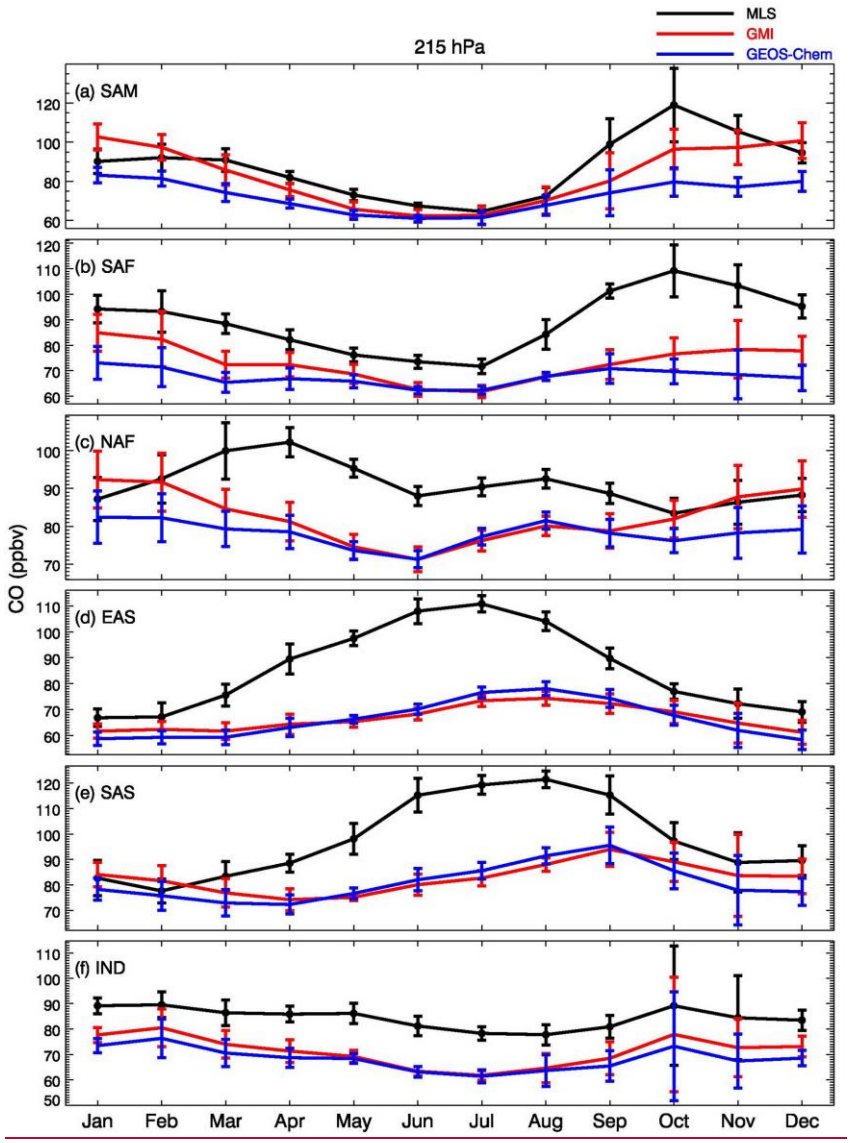

Fig. 12. Climatological (8-year) monthly mean of CO mixing ratio at 215 hPa from MLS V4 data (black line), GMI model simulation with MLS AKs applied (red line), and GEOS-Chem model simulation with MLS AKs applied (blue line) over the selected six

regions: (a) South America, (b) Southern Africa, (c) Northern Africa, (d) East Asia, (e) South Asia, and (f) Indonesia. The error bars indicate ±1 interannual standard deviation of the monthly mean CO from MLS ~~V4 data~~observation and model simulations.

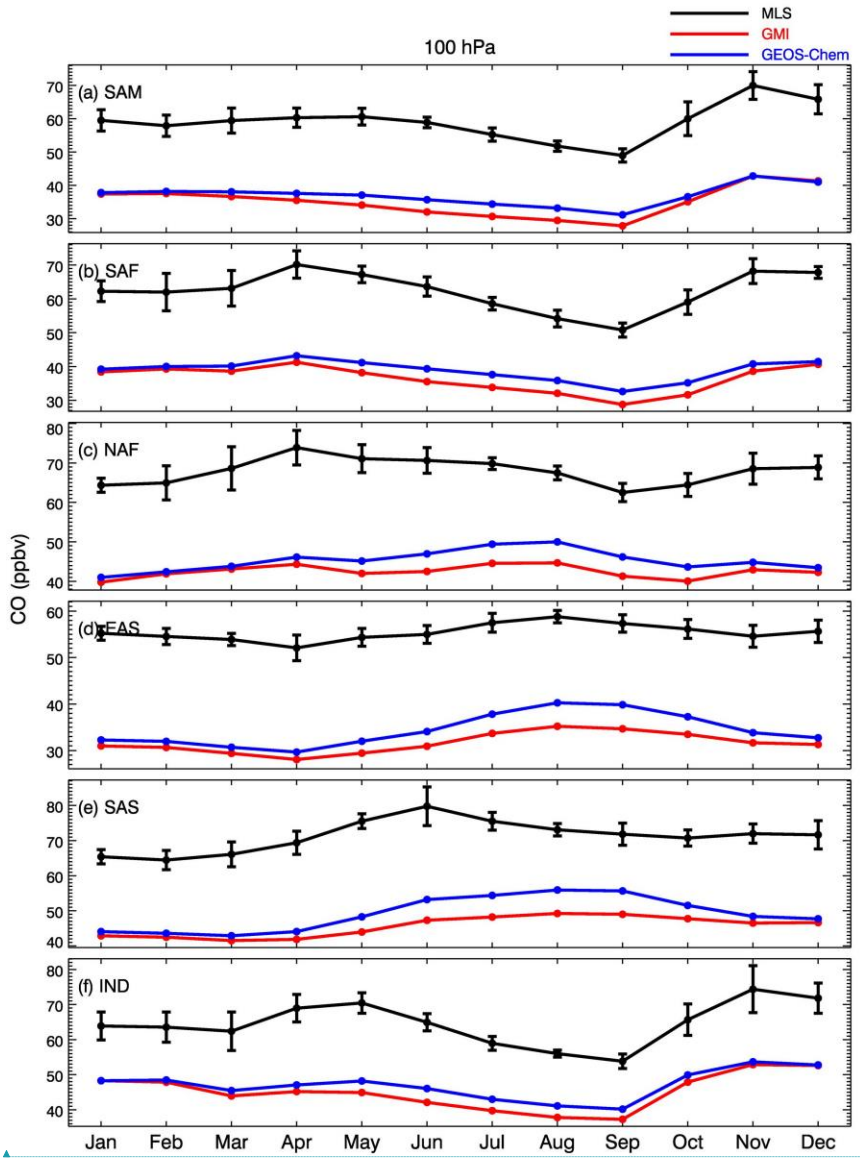

Formatted: Font: 12 pt

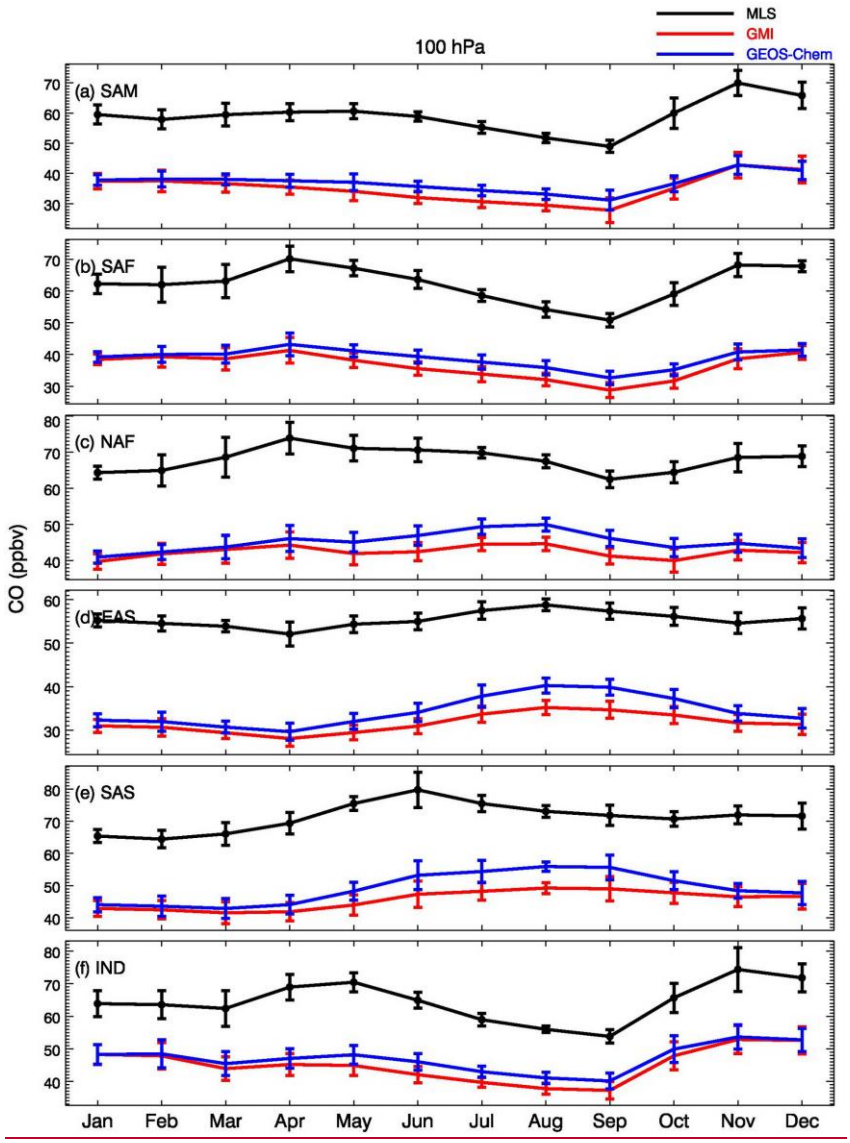

Fig. 13. As in Fig. 12, but for CO mixing ratio at 100 hPa.

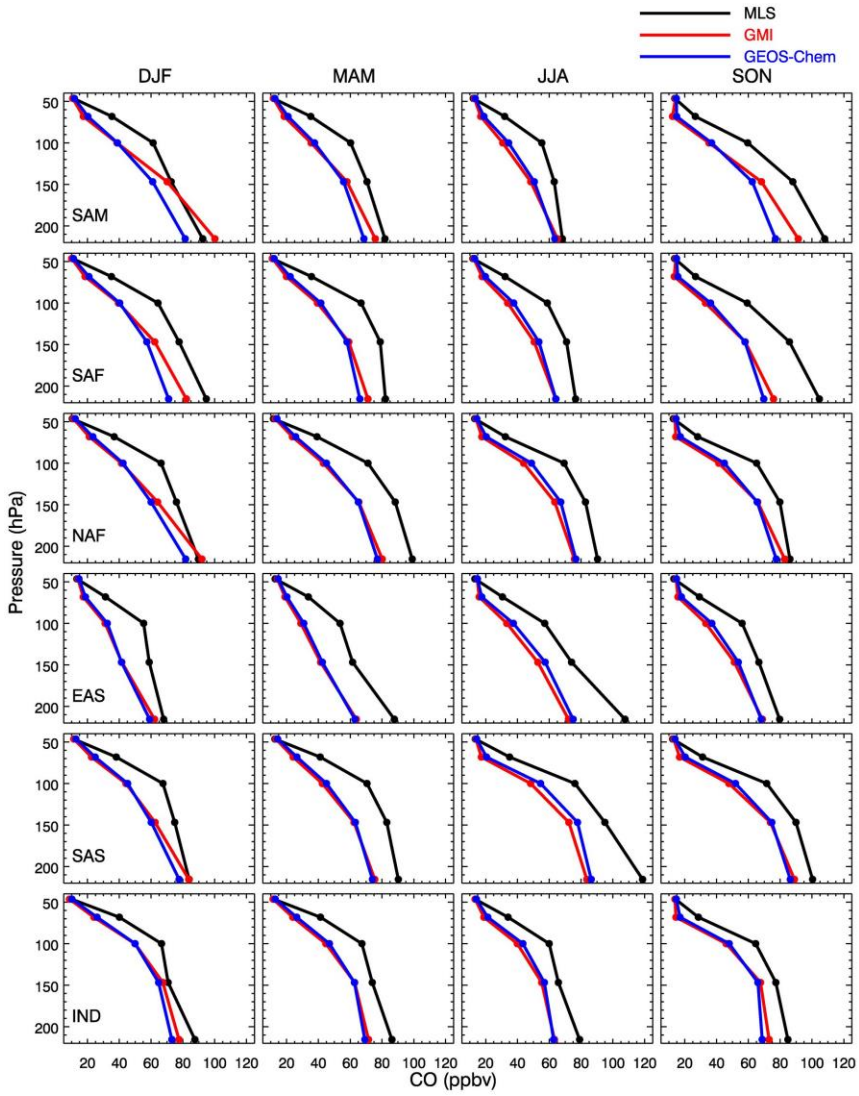

Fig. 14. Climatological (8-year) seasonal mean vertical profile of CO mixing ratio from MLS V4 data (black line), GMI model simulation with MLS AKs applied (red line), and GEOS-Chem model simulation with MLS AKs applied (blue line) over the selected six regions: (top row) South America, (second row from top) Southern Africa, (third row

from top) Northern Africa, (fourth row from top) East Asia, (fifth row from top) South Asia, and (bottom row) Indonesia.

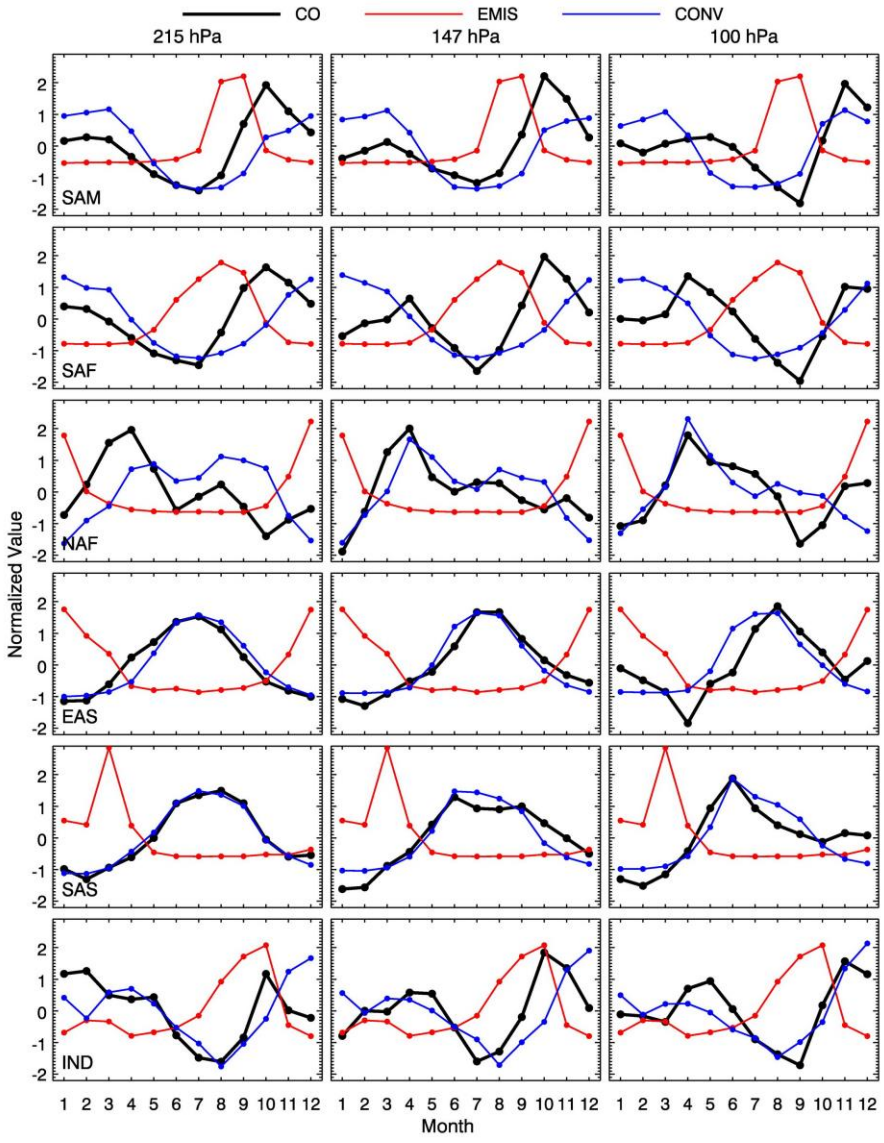

Fig. 15. Climatological monthly mean of surface CO emission from GMI model (red line), ice water content (blue line) and CO mixing ratio (black line) at 215 hPa (left column), 147 hPa (middle column), and 100 hPa (left column) from MLS observation over six regions: (top row) South America, (second row from top) Southern Africa, (third row from top) Northern Africa, (fourth row from top) East Asia, (fifth row from top) South Asia, and (bottom row) Indonesia. Each variable is normalized for comparison.

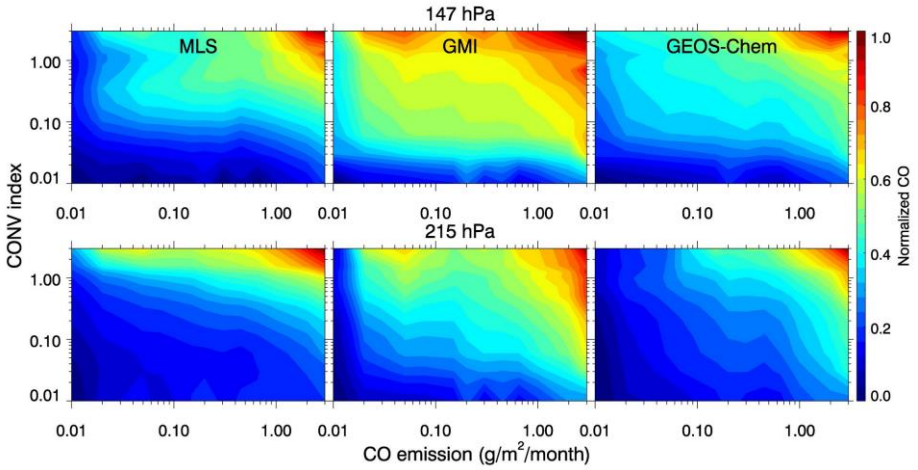

Fig. 16. Contour plots of normalized CO mixing ratio at 215 hPa (top row) and 147 hPa (bottom row) over the tropics (30°S–30°N) from MLS observation (left column), GMI model simulation (middle column), and GEOS-Chem model simulation (left column) binned according to the surface CO emission (x-axis) and convective index (y-axis) at the same pressure level. See text for more details.

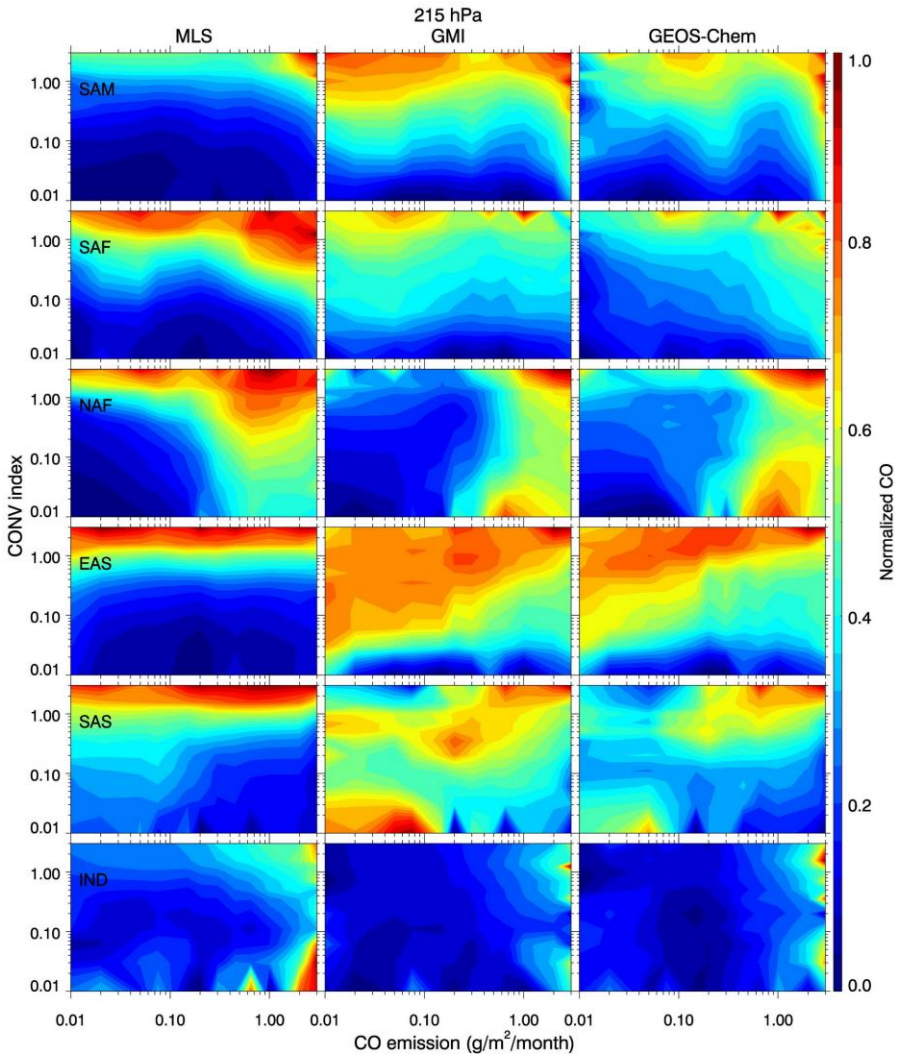

1138

1139 **Fig. 17.** Contour plots of normalized CO mixing ratio at 215 hPa over six regions: (top
1140 row) South America, (second row from top) Southern Africa, (third row from top)
1141 Northern Africa, (fourth row from top) East Asia, (fifth row from top) South Asia, and
1142 (bottom row) Indonesia, from MLS observation (left column), GMI model simulation
1143 (middle column), and GEOS-Chem model simulation (left column) binned according to

1144 the surface CO emission (x-axis) and convective index (y-axis) at the same pressure level.

1145 See text for more details.

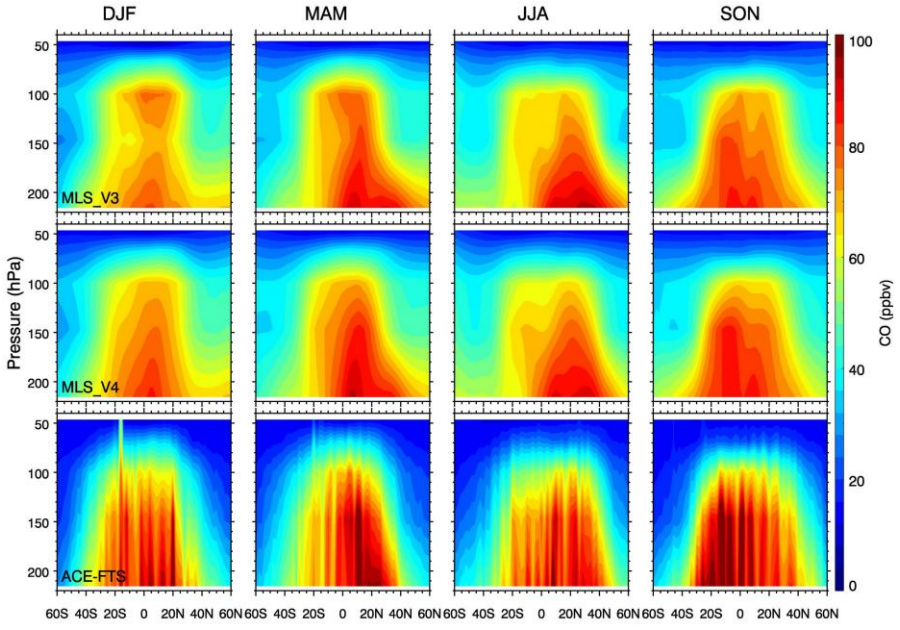

1146

1147 **Fig. A1.** Vertical distribution of zonal mean CO mixing ratio in the pressure-latitude

1148 cross-section during different seasons (DJF, MAM, JJA, and SON) from: (top row) MLS

1149 Version 3 CO data; (middle row) MLS Version 4 CO data; (bottom row) ACE-FTS CO

1150 data with MLS averaging kernels (AKs) applied.

1151

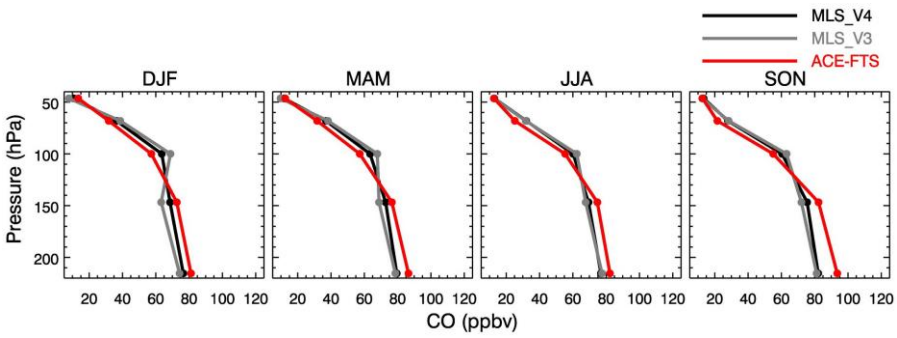

Fig. A2. Climatological (8-year) seasonal mean vertical profile of CO mixing ratio from MLS Version 4 CO data (black line), MLS Version 3 CO data (gray line), and ACE-FTS CO data with MLS AKs applied (red line) over the tropics (30 °S–30 °N).